MECHATRONIC ANALYSIS OF LIGHTWEIGHT ROBOTIC JOINTS

BACHELORARBEIT
von

Nico März

geb. am
29.11.1991
wohnhaft in
Wettersteinstr. 25A
82194 Gröbenzell
Tel.: 0176/39130274

Lehrstuhl für
STEUERUNGS- und REGELUNGSTECHNIK
Technische Universität München

Univ.-Prof. Dr.-Ing./Univ. Tokio Martin Buss

Betreuer:	Prof. Dongheui Lee, Prof. Sami Haddadin
Beginn:	20.02.2015
Zwischenbericht:	16.04.2015
Ende:	21.05.2015

– SIGNED EXERCISE SHEET –

Abstract

This thesis is located in the field of joint identification of robotic joint concepts. With focus on flexible joints, the appearing (electrical and mechanical) non-idealities of used components such as sensors and mechanical structures will be portrayed, and their relevance to the control of flexible joints in lightweight robots will be illustrated. For realistic modelling and compensation of several occurring non-idealities, the most popular strategies will be applied and parametrized. The results of the elucidated strategies will be validated on test benches with real joints, targeting an estimation of the case depending usability. The focus lies on friction compensation as well as position encoding. To parametrize control and non-ideality-compensation, (automated) test routines will be invented and implemented.

Zusammenfassung

Diese Bachelorarbeit entstammt dem Bereich Gelenkidentifikation an Robotergelenkkonzepten. Mit dem Fokus auf elastischen Gelenken werden auftretende mechanische sowie elektrische Nicht-Idealitäten der verwendeten Bauteile dargestellt, sowie deren Relevanz für die Regelung besagter Gelenke in Leichtbau-Robotern aufgezeigt. Für die realitische Modellierung sowie Kompensation einiger auftretender Nicht-Idealitäten werden verschiedene Methoden und Modelle parametrisiert und angewandt. Die Ergebnisse der verwendeten Strategien werden anschließend auf einem Teststand an realen Gelenken verifiziert. Der Fokus liegt hierbei auf den Bereichen Reibungskompensation und Positionsberechnung. Um die Parametrisierung und den Erfolg der Kompensation zu evaluieren werden (automatisierte) Testroutinen beschrieben und implementiert.

Contents

1 Introduction 5

1.1 Motivation 5

1.2 Contribution 5

1.3 Structure of Report 6

2 State of the Art 7

2.1 Rotary Encoders in Lightweight Robotic Joints 8

2.1.1 Rotary Encoder Concepts 8

2.1.1.1 Mechanical Encoder 8

2.1.1.2 Optical Encoder 8

2.1.1.3 Capacitive Encoder 9

2.1.1.4 Magnetic Encoder 9

2.1.2 Referencing in Relative Encoders 9

2.1.3 Data Transfer 10

2.2 Torque Sensors in Flexible Robotic Joints 11

2.2.1 Strain Gauge 11

2.2.2 Torsion Rod 11

2.2.3 Magnetostriction 12

2.3 Modelling of Friction in Lightweight Robotic Joints 12

2.3.1 Static Friction Models 13

2.3.1.1 Coulomb Friction 13

2.3.1.2 Load-dependent Friction 13

2.3.1.3 Viscous Friction 13

2.3.1.4 Static Friction and Break-Away Force 14

2.3.1.5 Stribeck Effect 15

2.3.1.6 All Static Models Combined 15

2.3.2 Dynamic Friction Models 15

2.3.2.1 The Bistle Model 16

2.3.2.2 The Dahl Model 16

2.3.2.3 The Lund-Grenoble Model 17

2.3.2.4 Further Dynamic Models 17

2.3.3 Usage of Friction Models 17

3 Joint Designs and Test Bench **19**
3.1 Schematic of Flexible Robotic Joints 19
3.2 Joint Test Bench 19
3.3 Joint prototypes 22

4 Modelling and Compensation of Non-Idealities **25**
4.1 Rotary Encoder 25
4.1.1 The Rotary Encoder Test Bench 25
4.1.2 Time Behavior of the Encoder 27
4.1.3 Linearity of the Sensor 29
4.1.4 Positioning of the Decoder Chip 29
4.1.5 Compensation 32
4.2 Friction Modelling and Identification 35
4.2.1 Measuring Static Friction 35
4.2.2 Coulomb and Viscous Friction 35
4.2.2.1 Model Parameterization 37
4.2.2.2 Model Verification 38
4.2.3 Complete Static Friction Model 38
4.2.4 Compensation with Static Friction Models 38
4.2.4.1 Coulomb Friction Model 41
4.2.4.2 Coulomb and Viscous Friction Model 41
4.2.4.3 Complete Static Friction Model 45
4.2.5 Compensation with Friction Observer 45
4.2.6 Comparison 46
4.3 Joint Flexibility 48
4.3.1 Measurement Method 48
4.3.2 Evaluation 49

5 Conclusion **53**
5.1 Summary 53
5.2 Conclusion 53
5.3 Outlook 54

List of Abbreviations **55**

List of Symbols **57**

List of Figures **59**

List of Tables **61**

Bibliography **63**

Chapter 1

Introduction

1.1 Motivation

Flexible, distributed, and smart automation, involving close and physical human-robot interaction (pHRI) has become one of the core concepts of the Industry 4.0 initiatives. Opening the compatibility between humans and robots is the final step in manufacturing using tactile robots. The ultimate goal is to have a flexible and dynamic production environment where robots and humans work side by side. One, if not the key enabler technology for this current trend is a fundamentally novel class of lightweight robots, as depicted in Fig. 1.1. The term lightweight robot refers to manipulators, which go beyond the classical payload-to-weight ratios of conventional industrial robots.

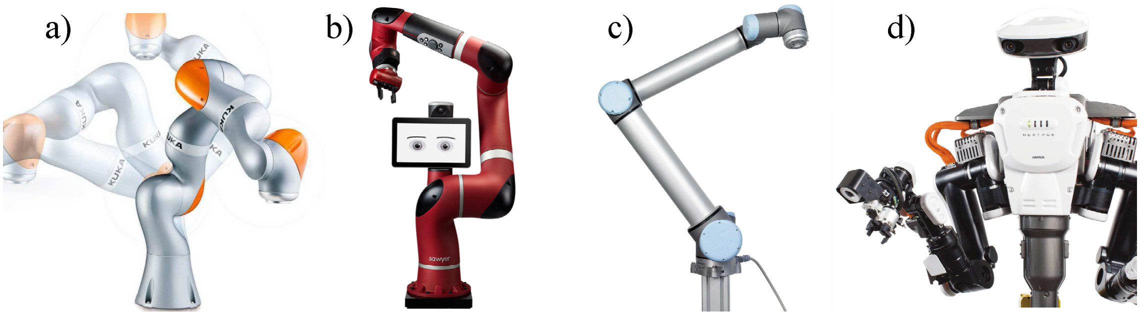

Figure 1.1: State of the art lightweight robots: a) KUKA's LWR iiwa, b) Sawyer™from Rethink! Robotics, c) UR5/10 from Universal Robots, d) KAWADA's NEXTAGE®

1.2 Contribution

This thesis provides analysis and improvement suggestions for several flexible lightweight robotic joint components. The individual components were inspected with regard to possible non-idealities and interfering influences. With focus on mechanical issues, these non-idealities have been analysed. The main focus lies on friction as well as flexibility influences and possible position complications. These points were regarded towards consequence and compensability. While the position error compensation is quite straightforward, for friction compensation, multiple approaches are discussed and evaluated. All strategies are verified on two lightweight robotic joint designs on different test benches.

1.3 Structure of Report

The thesis is structured the same as the usual way of development. First, most of the used parts will be presented. Then, several occurring issues and problems will be regarded concerning their relevance to the system and the possibilities of counteractions.

In chapter one, a rough overview over the most important non-idealities that will occur in flexible joints will be given. They will be quantified in the next two chapters, considering several measurements and empirical data. The fourth chapter will illustrate the possibilities, to compensate the mentioned non-idealities with regard to flexible joint control. The previously mentioned compensation strategies will be verified with mechanical experiments the basis of two different flexible joint designs.

Chapter 2

State of the Art

Within the development of industry 4.0 ([1] provides a rough overview for this topic), which is practically the co-working of robots and humans side-by-side in multiple fields [2], small and preferably cheap robots are more and more required in industrial and social environments [3]. In [4] the evolution and further possibilities of this field are discussed. Here, only the small field of lightweight robots will be regarded, respectively their main inner parts, the joints, will be identified.

As already discussed in several proceedings and theses [5], [6], [7], [8], robotic joints contain mostly the mechanical and electrical parts. The joint is driven by an electrical actuator (**motor**). Commonly used are brushless direct current (BLDC) motors which have been discussed and analysed for that application in [9], [10] (among many others). Therefore, their analysis will not be part of this thesis. They can be driven by any digital signal processor (DSP) with field oriented control (FOC) or direct torque control (DTC) [11], [12], [13]. For this control, the acquisition of the current motor position is necessary. This is done either with a dedicated sensor (**rotary encoder**) or with complex angle detection mechanisms [14], [15]. In the examined case, only the dedicated encoders will be attended, as they are used in the targeted joints.
Either the joints are designed as *direct drive* which attaches the link directly to the motor strain (see e.g. [16]), or a **gear-train** is attached downstream. For the gear, multiple designs are common. Widely used are transmissions of the type strain wave gear (SWG), as described in [17], [18] because of their lightweight structure and high gear ratio with small form factor. Equally light but bigger are belt transmissions. They are well-analized in many publications [19], [20], [21], [22] and used in all kinds of machines. The two joint concepts for identification (see Sec. 3.3) provide belt drives as well as strain wave gearings. Mostly, there are no more structural mechanical parts than the mentioned ones.
For control, additional sensors are required. Since the joints are designed to be lightweight, a high amount of flexibility inside the joint is implied. Therefore, the real link position is needed for controlling as well as the applied torque in form of load, gravitation or inertia. To measure this impacts, an additional rotary encoder can be used, as well as a **torque sensor**. Both sensors will also be discussed further.

Additional sensors and actuators, such as a mechanical brake, are mostly optional and will not be regarded.

2.1 Rotary Encoders in Lightweight Robotic Joints

For controlling positions in robotic joints it is indispensable to get an exact feedback of the real current position. Although a rough estimation can be given by other sensor values and past movements, this calculations can never be good enough to precisely control a joint. Therefore, an external sensor for position measuring is required. Those sensors are commonly known as *rotary encoders*, as they transform any position on the rotating axis into a digital value.

Depending on the requirements such as speed, precision or environment, a wide range of capturing methods and designs have been developed [23].

2.1.1 Rotary Encoder Concepts

Said requirements cause a wide range of different designs. The most popular ones will be described in this chapter. Position encoders can be designed either as absolute encoder, that means without initialisation, the real position is provided, or relative, that means only position differences will be measured. Relative position encoder designs often provide an additional signal for reference positions.

2.1.1.1 Mechanical Encoder

An encoder implementation with brushes works pretty much like a rotary switch. Multiple brushes move on interrupted metal plates. This structure is very cheap, but has several disadvantages. The brushes are not arbitrarily scalable, which reduces the maximal precision, every brush has to be de-bounced, either via additional hardware or software, and all mechanical parts have a strong wear-out. This concept can either be designed absolute with one brush per bit resolution; or relative with or three brushes on interrupted contact zones for direct quadrature encoder pulse (QEP) output.

2.1.1.2 Optical Encoder

A perforated disc interrupts a (light-) beam between a light-emitting diode (LED) and a light dependent resistor (LDR) or photo-transistor. Some systems may use other light gates, but this combination is to some extent standard. In relative sensors, with two independent light barriers in a distance of half a stripe (shifted 90°) may be used directly as QEP output (see Sec. 2.1.3). This kind of sensor has no latency as long as speed of light and signal transmission can be assumed as instant. Though it would be possible to use one light barrier per bit for absolute design, this concept is commonly manufactured as relative encoder only.

2.1.1.3 Capacitive Encoder

In capacity encoders, the rotor disk looks like the one in optical encoders, but with a dielectric instead of the light blocking stripes. It is rotated between two plates to create a capacitor with variable capacity. This allows a much more precise measurement, since the stripes do not generate a simple on/off-signal, but a continuously changing capacity. By using this information, the number of required stripes can be reduced dramatically at the cost of increasing calculation effort and therefore a small latency. As it is inevitable to use a microchip to create the output signals, most sensors of this kind have an additional output via a serial protocol for errors and absolute positions. Absolute encoders can also be designed with two irregularly shaped plates, that are rotated against each other, generating an unique capacity at each position. Therefore, this concept allows absolute position calculation.

2.1.1.4 Magnetic Encoder

Based on the measurement of magnetic fields, (mostly with hall effect sensors [24]) the position of a magnetic target can be evaluated. Commonly, multiple magnetic poles can be placed to enlarge the resolution [25]. For further precision enhancement, an additional trace of poles can be used as nonius. This measurement method requires calculation, so that encoder circuits usually cause a delay of several μs. Same as the capacitive encoder design, based on the unique calculated position, this design provides absolute position information.

2.1.2 Referencing in Relative Encoders

In positioning systems, it is usually necessary to be able to calculate an absolute position, at least to define a starting offset. This is commonly achieved by a so called index-bit (or zero-bit) which is usually labelled as X or Z, that resembles a defined position, which is commonly 0.

Linear Encoders offer multiple ways of determining an absolute position. For conveyor systems, it might be the easiest and safest, to set reference marks as endpoints of the moving range. Though this implies two reference marks, their position can be unified by considering the driving direction. This system is only faulty, if the moving part powers down (or whatever it needs to loose its position knowledge) directly on the reference mark. Mechanical structures can avoid this problem, for example by using tongued endpoints, so that the marks can only be reached by applied force. The guaranteed possibility to run both directions, even without knowing the exact position makes this structure error-proof and self-sufficient. In contrast, a single zero-mark in the middle of the range would force surveillance if it is required to power up the system in an unknown position. A third possibility is a set of marks coded by their distance (distance coded reference marks (DCRM)). As long as the distances are unique, the absolute position can be recognized after passing two marks. This method is equally vulnerable to the previous mentioned single mark at

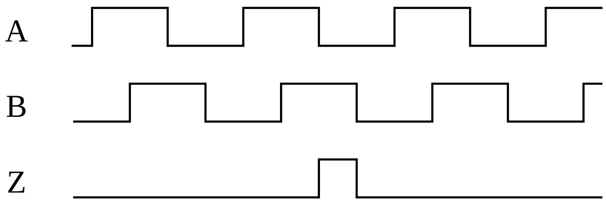

Figure 2.1: Typical QEP signal with index mark at steady velocity

starting after losing the absolute position. In **rotative encoders**, the index indicator usually appears once per revolution. Doing so, one revolution has to be endurable during initiation. For some use-cases, a solution with two end-marks (as mentioned above) may be preferable. It guarantees to not exceed physical limitations at the expense of complete revolutions.

2.1.3 Data Transfer

The incremental position is usually transmitted by QEP which is a two channel (with index signal three channel) binary protocol. Every edge resembles one increment. Both wires contain the same signal, but with 90° phase shift. This allows four times higher resolution (quadrature) and direction recognition. A typical signal is shown in Fig. 2.1. Quasi-standard for transmission are transistor–transistor logic (TTL) and high threshold logic (HTL). Alternatively, instead of binary signals, analogue signals in sinoid shape can be used. This allows much better interpolating, but is not possible with all scanning principles. If absolute positions are available, they are commonly carried by serial interfaces, such as serial peripheral interface (SPI), RS 232, synchronous serial interface (SSI), or Universal Asynchronous Receiver Transmitter (UART).

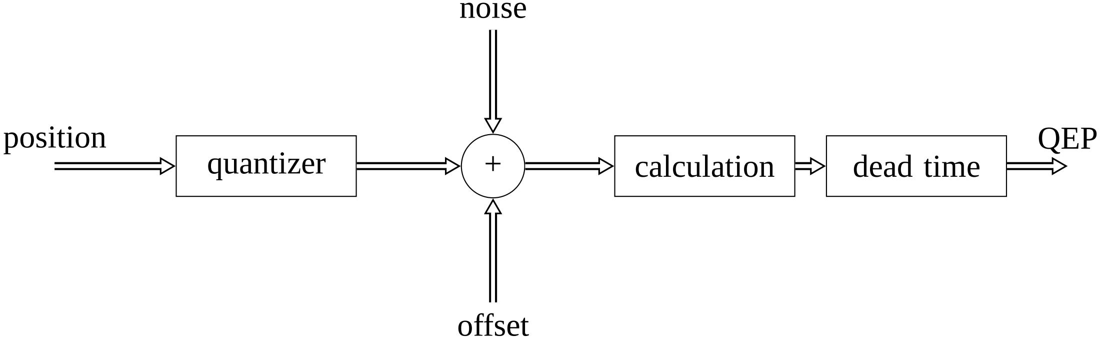

Figure 2.2: Schematic of data acquisition chain in rotary encoder application

2.2 Torque Sensors in Flexible Robotic Joints

The second important field of used sensor appliance is torque measurement. In flexible joints, structural parts of the joints often bend due to the applied torque. This, and the importance of knowledge of the load and other influences for controlling make the sensing of torque an not negligible part of the control chain. Figure 2.3 presents the schematic of the data acquisition chain in most torque sensors.

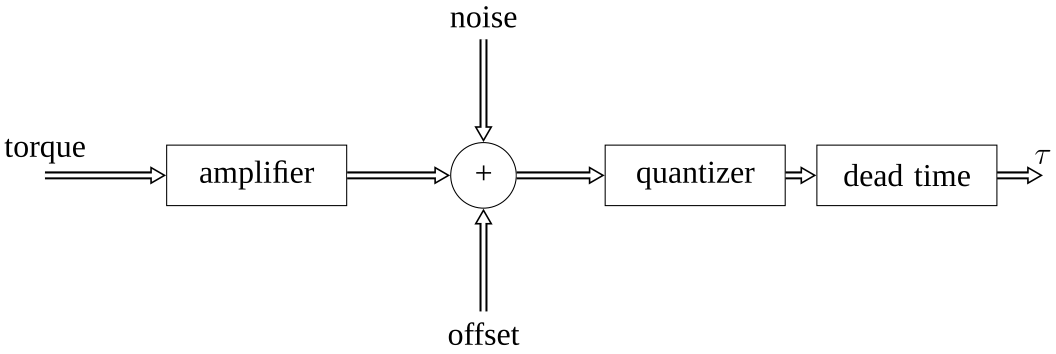

Figure 2.3: Schematic of data acquisition chain in torque sensor application

Torque is commonly measured via a bending or twisting part of the force leading structure. There are several different methods and designs, that are listed hereafter.

2.2.1 Strain Gauge

The working principle is based on changing resistance in mechanically stressed materials. Some materials have a linear dependency of elongation and resistance, and are therefore well suited for this purpose. For wiring, metal or semiconductors are commonly used, whereby semiconductors are more sensitive, but in high load situations nonlinear. The schematic structure of a typical strain gauge can be seen in Fig. 2.4. To eliminate temperature and shear force influences, multiple strain gauges are often wired as a Wheatstone bridge [26]. Thereby, the influences compensate each other, as only differences between two gauges, arranged in rectangular form, is measured.

2.2.2 Torsion Rod

Both rotary encoders are mounted at the ends of the torsion rod. When torque is applied, the rod is twisted. This leads to a measurable difference in the received position. In small angles ($\phi < 3°$) the relation between torque τ and torsion ϕ can be approximated as linear. In reality, the twisted angle is targeted far below $1°$. This requires the sensor to have a high dynamic range, paired with low noise and high resolutions. This is the most frequent exclusion criterion in low-cost solutions.
Also, the calculation of the applied torque can start after both sensors have processed their

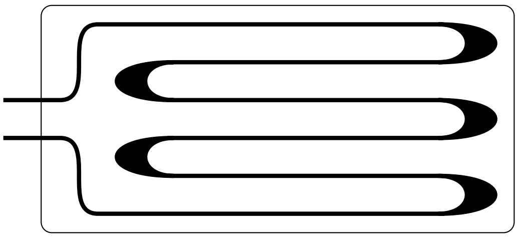

Figure 2.4: Schematic strain gauge. The stress direction in this picture would be horizontal

data. This, in addition to the required calculation time for the torque itself, leads to further delay and therefore to slower controlling.

2.2.3 Magnetostriction

Magnetostriction, also known as the Villari effect ([27]), is one of the few physical effects, that could also be used for torque detection. While magnetostriction originally characterizes the material behavior in changing magnetic filed, the *inverse magnetostrictive effect* describes the changing magnetic behavior of an mechanically stressed material.

2.3 Modelling of Friction in Lightweight Robotic Joints

Friction is an important aspect in all mechanical systems since it is present whenever two surfaces are in contact with each other. Especially in lightweight robots with high gear ratios this can lead to steady state errors, limited cycles and reduced performance. Friction is a highly nonlinear phenomenon and therefore difficult to model correctly. A large number of possible friction models for robots (and in general) can be found in literature [28], [29], [30]. By modeling friction with high accuracy its effects could be easily compensated based on model values. But on the other hand, highly accurate friction models are very complex and have to take into account temperature and other time-dependent environmental influences, which makes them very difficult to use in practical applications.

Several static friction models have been discussed widely in literature. They describe different friction effects based on the motor velocity, like viscous friction, Coulomb friction or the Stribeck effect [30] . Furthermore, a load-dependent friction model that relies on the measured joint torques is regarded. A good overview of known models and compensation methods is provides by [31].

Note, that friction can be treated equivalently as torque τ_f [Nm] or force f_f [N], as long as they are not mixed up.

2.3.1 Static Friction Models

The static friction models are the most basic and common friction models. They consist of different components, which each take care of certain aspects of the friction force. Those models are called static, as they contain no state variables nor differential equations, therefore are not time-dependent.

2.3.1.1 Coulomb Friction

The Coulomb friction model (definition and applications in [32]) is the simplest static friction model. It describes a constant friction force opposing any motion,

$$\tau_f = \tau_c sign(\dot{\theta}). \tag{2.1}$$

The force is independent of velocity magnitude. As it depends only on the direction of the motor velocity, the model has a discontinuity at zero velocity (see Fig. 2.5) which is generally covered by stiction force (Sec. 2.3.1.4).

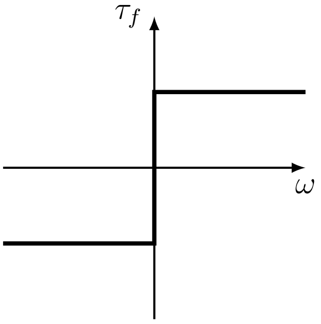

Figure 2.5: Coulomb friction model

2.3.1.2 Load-dependent Friction

In most types of transmissions, friction increases with load. This may vary widely for different kind of materials, and would be modelled empirically, since the variations throughout all materials would be too complex for a usable model. Figure 2.6 shows the effect for a linear and a square dependency.

2.3.1.3 Viscous Friction

The viscosity of lubricants causes a friction that depends on the velocity. This friction is called viscous friction,

$$\tau_v = c_v \dot{\theta}_m, \tag{2.2}$$

and can be modelled using the motor velocity and a constant viscous coefficient c_v, see Fig. 2.7.

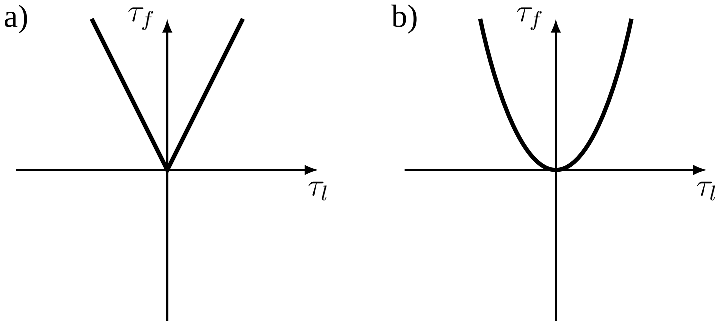

Figure 2.6: Load-dependent friction linear (a) and square (b)

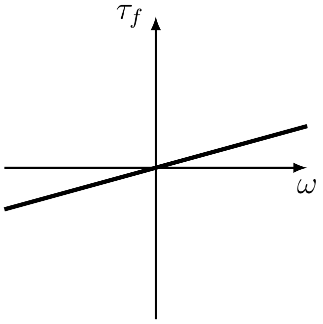

Figure 2.7: Viscous friction model

2.3.1.4 Static Friction and Break-Away Force

Static friction (or short *stiction*) describes the friction force at rest. The force required to overcome the static friction and initiate motion is called the break-away force τ_h. It is commonly higher than the coulomb friction. Fig. 2.8 shows a combined model for static friction, Coulomb friction and viscous friction. After the force exceeds the break-away force the friction instantly drops to the Coulomb friction level. It is modelled as a function of the external force f_e and the static limiting force f_{sl}.

$$f_h = \begin{cases} f_e & \text{for} \quad \dot{\theta} = 0 \quad \text{and} \quad \mid f_e \mid < f_{sl} \\ f_{sl}\,\mathrm{sgn}(f_e) & \text{for} \quad \dot{\theta} = 0 \quad \text{and} \quad \mid f_e \mid \geq f_{sl} \end{cases} \tag{2.3}$$

The maximum friction force typically occurs at a small displacement from the starting point. Stiction in combination with coulomb and viscous friction is shown in Fig. 2.8.

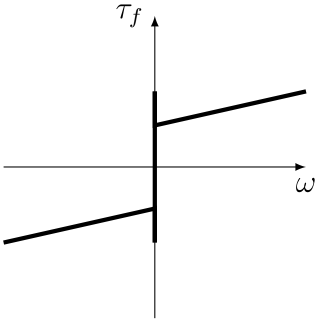

Figure 2.8: Friction model with coulomb, viscous and static friction

2.3.1.5 Stribeck Effect

R. Stribeck described 1903 in [33], that for slow velocities, the stiction does not drop instantly with overcoming f_s. The real curve can be described as an exponential decrease

$$\tau_s = (f_h - f_c)e^{-\left(\frac{|\dot{\theta}|}{v_s}\right)^{\delta_s}}. \tag{2.4}$$

with f_h as stiction (see Sec. 2.3.1.4), f_c as coulomb friction (see Sec. 2.3.1.1), and v_s as the so called stribeck velocity, an empirical parameter to characterize the curve. For most modulations, δ_s is set to 2. If this effect is modelled as stribeck friction τ_s, it includes the stiction torque as well.

2.3.1.6 All Static Models Combined

All mentioned phenomena are independent, therefore they can be added up to generate a complete model of the total amount of static friction. This summed up model is very often used for evaluation and compensation in robotics. Two examples of typical usage are presented in [34] and [35],

$$\tau_f = (\tau_c + \tau_s)\,\mathrm{sgn}(\dot{\theta}) + \tau_v, \tag{2.5}$$

$$\tau_f\left(\dot{\theta}\right) = \left(\tau_c + (\tau_h - \tau_c)\,e^{-\left(\frac{|\dot{\theta}|}{v_s}\right)^{\delta_s}}\right)\mathrm{sgn}\left(\dot{\theta}\right) + c_v\dot{\theta}_r. \tag{2.6}$$

The according plot can be seen in Fig. 2.9.

2.3.2 Dynamic Friction Models

The friction phenomena related to non-stationary velocities, small displacements occuring during the stiction phase, and hysteresis effects can be captured only by the time-variant, **dynamic** models.

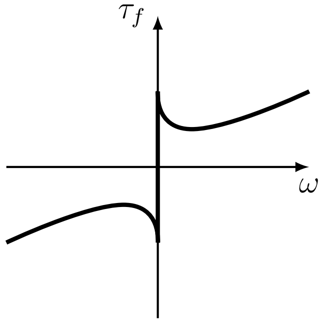

Figure 2.9: Complete static friction models with stribeck effect

2.3.2.1 The Bistle Model

Haessig and Friedland introduced a friction model in [36], which attempted to examine the behavior of the microscopical contact points between two surfaces. Due to irregularities in the surfaces the number of contact points and their location are considered as random. Each contact point is interpreted as a bond between flexible bristles. As the surfaces move relative to each other the strain in the bond increases and the bristles act as springs giving rise to a friction force. The force is then given by

$$f_b = \sum_N \sigma_0(x_i - b_i), \tag{2.7}$$

where N is the number of bristles, σ_0 the stiffness of the bristles, x_i the relative position of the bristles, and b_i the location where the bond was formed. As $|x_i - b_i|$ equals δ_s the bond snaps and a new one is formed at a random location relative to the previous location. The complexity of the model increases with N. Usable results were found with 20 to 25 bristles, but even a single bristle gave reasonable qualitative behaviour. The stiffness of the bristles, σ_0, can be made velocity dependent. An interesting property of the model is that it captures the random nature of friction. The randomness depends on the number of bristles. The model is inefficient in simulations due to its complexity. Also, since there is is no damping of the bristles in the model, motion in sticking may be oscillatory.

2.3.2.2 The Dahl Model

The model of Dahl, illustrated in [37] is well-known as the simplest possible way to describe the dynamic behaviour,

$$\dot{z} = v - \frac{|\, v \,|}{f_c}\sigma z, \tag{2.8}$$

$$f_d = \sigma z, \tag{2.9}$$

where σ represents the bristle stiffness and z the average bristle deflection. This model is simplified to the time-variant part, as the used bristle friction is just the coulomb friction, discussed in Sec. 2.3.1.1.

2.3.2.3 The Lund-Grenoble Model

The Lund-Grenoble model is a dynamic friction model presented in [38]. It can be seen as expansion of the Dahl model, replacing the coulomb friction f_c with a more complex approximation. Similar to the bristle model, it interprets every contact point individually. All bristols are modelled as ideal springs with stiffness $\sigma_0 > 0$. To oppress oscillation (unlike Sec. 2.3.2.1), the damping coefficient $\sigma_1(\omega)$ is used. Regarding Sec. 2.3, the unit of σ_x can either be, [Nm/rad] or [N/m], depending on the scenario. The mean bristle deflection is labelled z ([rad] or [m]).

$$f_{lg} = \sigma_0 z + \sigma_1 \dot{z} + \alpha_2 \dot{\theta}, \tag{2.10}$$

$$\dot{z} = \dot{\theta} - z \frac{\mid \dot{\theta} \mid}{g(\dot{\theta})}, \tag{2.11}$$

$$g(\dot{\theta}) = \alpha_0 + \alpha_1 e^{-\left(\frac{\dot{\theta}}{v_s}\right)}. \tag{2.12}$$

These equations are able to handle the stribeck effect as well as time-dependent stiction. For the steady state, the LuGre model reduces to the well-known static equation

$$g(\dot{\theta}) = \frac{1}{\sigma_0} \left(\tau_c + (\tau_h - \tau_c)\, e^{-\left(\frac{\dot{\theta}}{\dot{\theta}_s}\right)^2} \right). \tag{2.13}$$

2.3.2.4 Further Dynamic Models

Dynamic models can be very complex (a rough overview is given in [39]), but for the application in the targeted robot system, the mentioned models are more than sufficient.

2.3.3 Usage of Friction Models

For most use-cases, the **static equation(s)** provide sufficient information about the occurring friction. Several use-cases even use just the coulomb friction (see Sec. 2.3.1.1). Since all equations are very straight forward, and only rely on a few measurable variables (velocity $\dot{\theta}$ and, if important, load τ_l or temperature. Thanks to the invariant dependencies, the static model can be provided in every complexity as a simple look-up table. This makes it attractive for fast and resource saving controlling. To model micro movement and precise time dependency, the **dynamic models** are necessary. They provide more precise information, and include (in the case of Lund-Grenoble Sec. 2.3.2.3) all static equations as well.

For compensation modelling in the real joints, an approximation via the static models is sufficient. This is because of the limited resolution of the position encoders, that limits the absolute precision. The additional information provided by the dynamic models is several orders of magnitude below the measurable precision.

Chapter 3

Joint Designs and Test Bench

3.1 Schematic of Flexible Robotic Joints

Flexible robots usually consist of three to seven individual joints. Typically, every joint has an independent control unit, that communicate via a bus with the top-level control interface. The individual control is placed on the Motor Control Board (MCB). There control units each consist of a powering unit for motor driving, several sensor inputs, and a central processing unit (CPU). Figure 3.1 provides a mechanical simplified model of a typical flexible joint with sensors. The marked ratings are each measured directly or indirectly via individual sensors.

3.2 Joint Test Bench

For the joint identification, a test bench is required. The used test bench was built according to S. Dendorfer [40]. It consists of two hysteresis brakes (4,6) for load simulation, a torque sensor (3) as reference, and an additional position encoder (2). The design provides two brakes, as it is designed for loads between 0 and 80 Nm. This can only be accomplished by two brakes, since one of them is only capable of $.15$ Nm. The second brake is enhanced by the gear train by factor 10. Further information is provided in proceeding. The mechanical parts are listed below, sorted from left to right (see Fig. 3.2):

Initializing the Load

Hysteresis brakes are designed to guarantee constant torque at all speeds. The *Mobac HB-1750M-2* is rated up to 6000 rpm, much more than needed. This is tested with one brake, without the downstream transmission and additional brake, using the velocity profile in Fig. 3.3. As it can be seen in Fig. 3.4, the *Mobac HB-1750M-2* is fully meeting expectations concerning velocity independency.
Reattaching the gear and the second brake, several disadvantages are revealed: First of all, the transmission has a breakaway torque of estimated 10 Nm. This makes less stressed

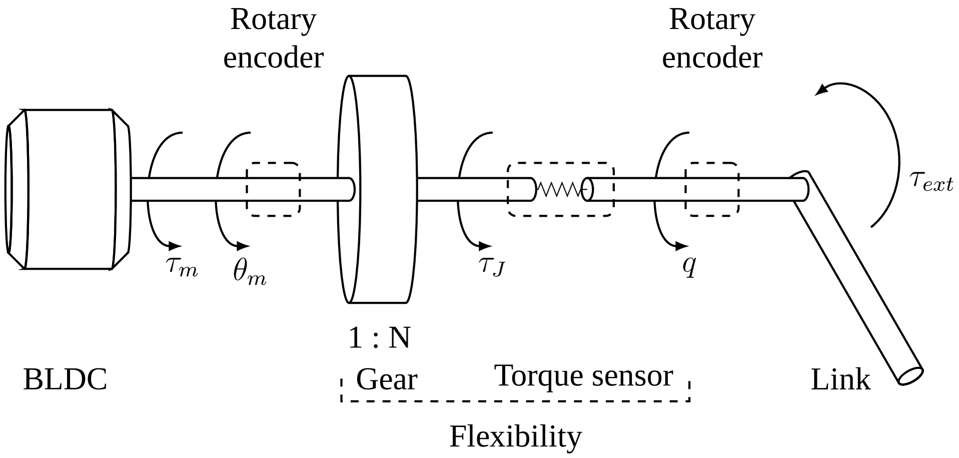
Rotary encoder
Rotary encoder
τ_{ext}
τ_m
θ_m
τ_J
q
1 : N
BLDC
Gear
Torque sensor
Link
Flexibility

Figure 3.1: Mechanical schematic of joint structure

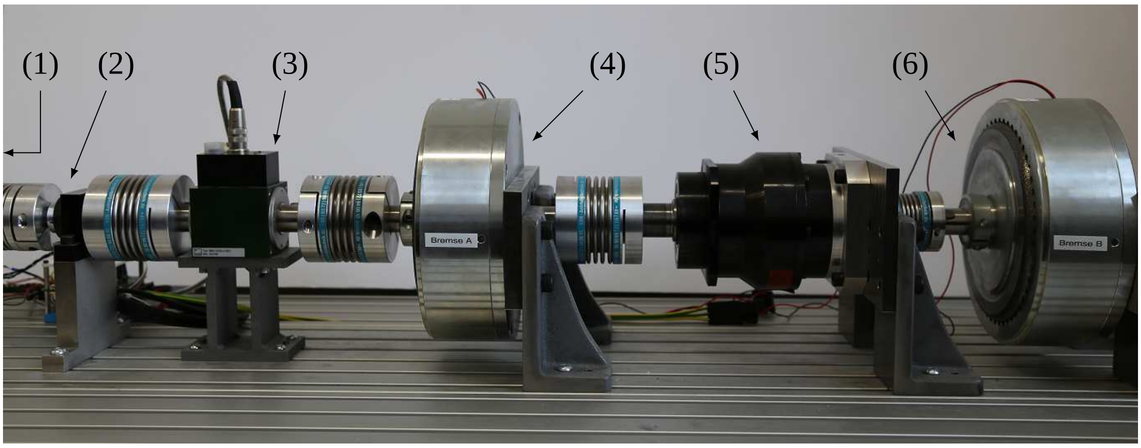
(1)
(2)
(3)
(4)
(5)
(6)
Bremse A
Bremse B

Figure 3.2: Picture of the joint identification test bench; The numbers are described in Tab. 3.1

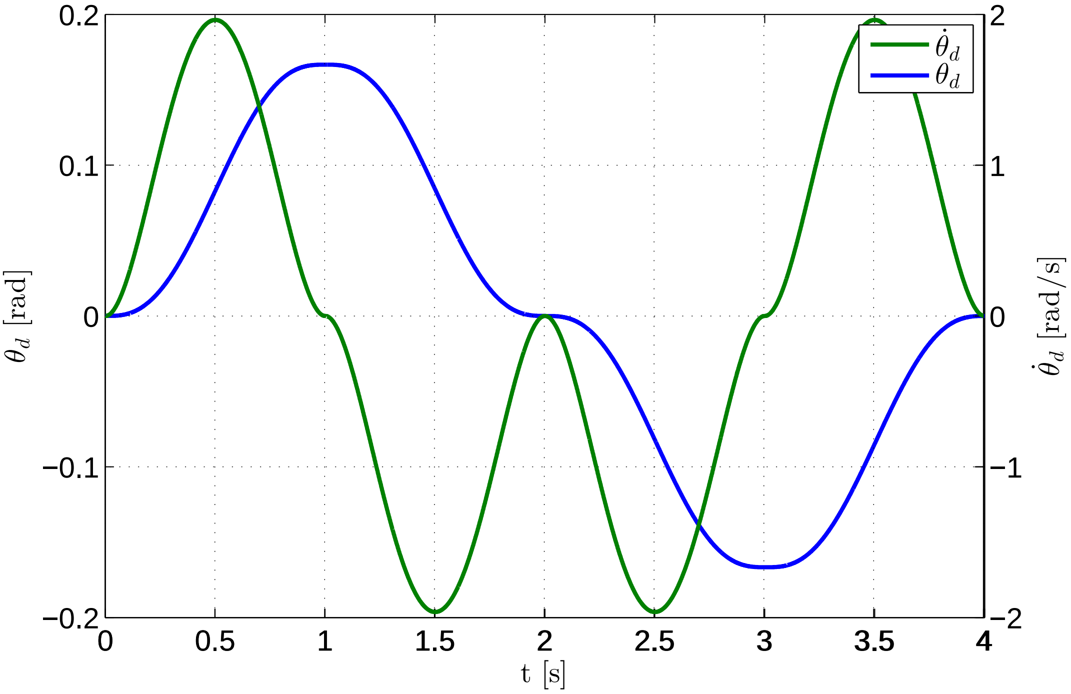

Figure 3.3: Position and speed profile for testing

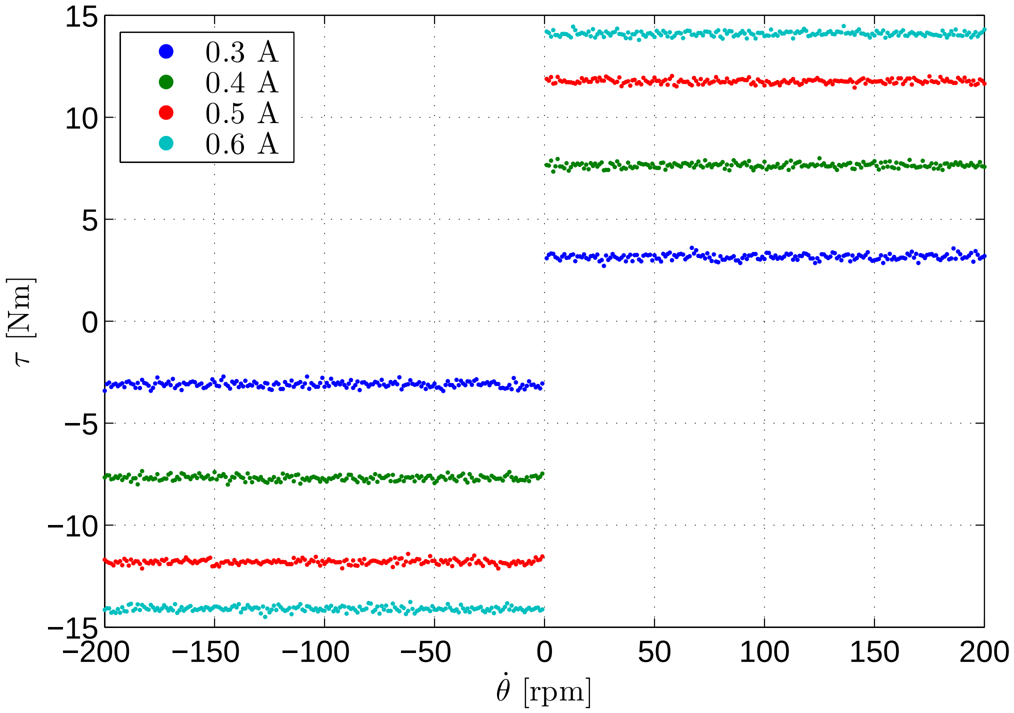

Figure 3.4: Hysteresis brake torque-speed dependency

No.	function	item	parameter
1	joint module	tested joint	A or B
2	rotary encoder	ASM Pmir4-20-64 O/M-83 ASM Pmis4-50-2048-50KHZ-TTL-Z1	16 poles 19 bit
3	torque sensor	Burster 8661-5200-V1002	0-200 Nm ± 0.05 % 0-20 Nm ± 0.1 %
4	hysteresis brake	Mobac HB-1750M-2-4651	rated 0-15 Nm
5	gear	TANDLER	1 : 10
6	hysteresis brake	Mobac HB-1750M-2-4651	rated 0-15 Nm

Table 3.1: Mechanical overview of the joint test bench

testing scenarios more elaborately, as the transmission has to be separated, and automated full-range measurements impossible. The gears velocity-friction behaviour (as it can be seen in Fig. 3.5) is completely non-linear and appears not to be easily compensated. For tests with a high and precisely known load, the concept brake-transmission-brake is not usable in this context. It may be an emergency solution for high loads on constant velocity, but then the brakes current has to be readjusted at every speed to allow consistency. The partially lower brake torque with downstream transmission and brake can be explained by the high inertia of the second brake and the transmissions flexibility.

Both brakes have a nearly identical current-torque correlation. As it can be seen in Fig. 3.6, the curve has a wide hysteresis. Because of this hysteresis, it is much more complex to control a static torque load. Due to that, most identification procedures will only have a stepped or sweeping control current. In most scenarios, it is only important to capture all possible brake torques, so that a current sweep is sufficient. Just for long term load testing, there will have to be an exact adjustment, but only for each single test.

3.3 Joint prototypes

Two different joints are available for testing. They are both typical designed for usage in lightweight robots, as they are optimized for weight and size. For driving, a BLDC motor is used, because of its high torque-per-weight ratio. Both joints contain two independent position encoders. While for joint A, two identical magnetic sensors are used, joint B is controlled with two optical encoders. Each encoder provides a resolution of 12 bit. The specifications can be compared in Tab. 3.2:

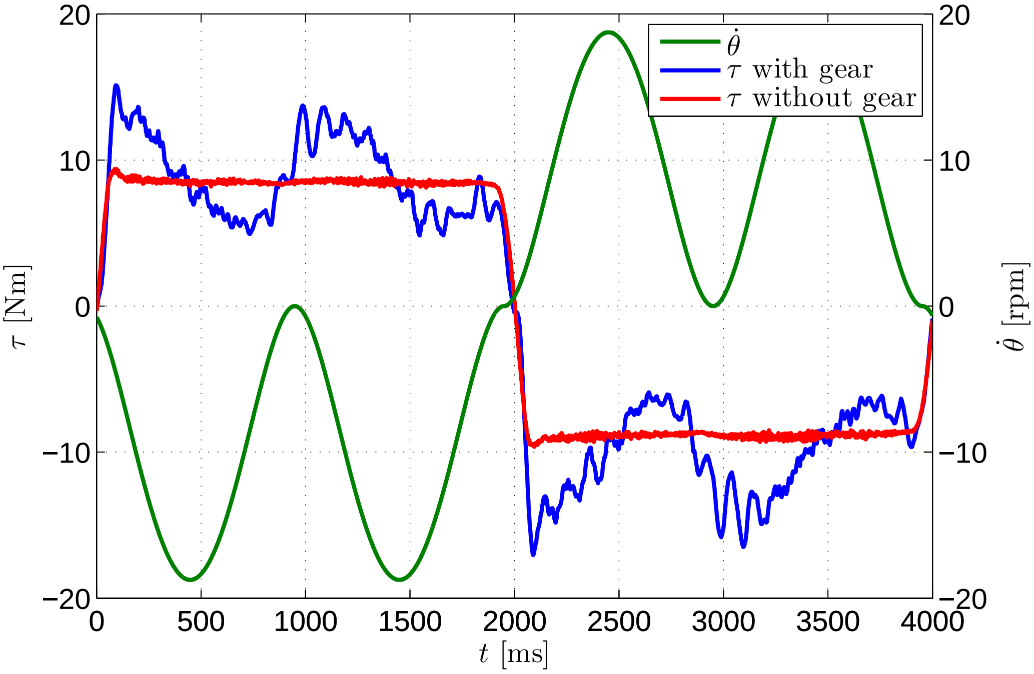

Figure 3.5: Torque at variable speed with and without transmission

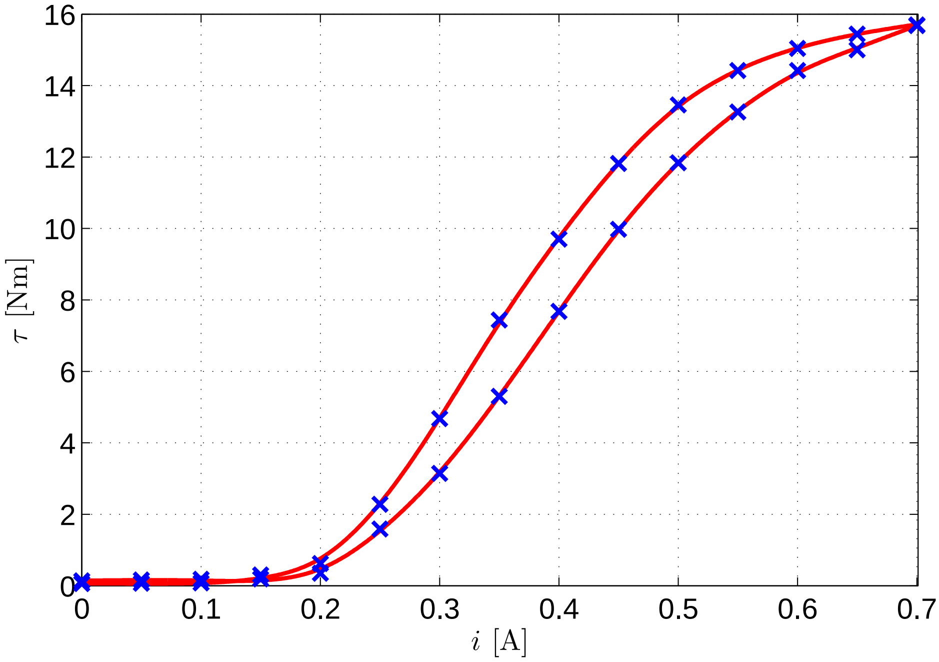

Figure 3.6: Hysteresis brake current-torque dependency

	joint A	**joint B**
motor type	BLDC	BLDC
torque constant k_m	0.0406 Nm/A	0.0798 Nm/A
first stage		
type	belt	belt
transmission	$40 : 18$	$150 : 18$
second stage		
type	SWG	belt
transmission	$80 : 1$	$72 : 12$
total		
transmission	$177.8 : 1$	$50 : 1$
rotation range	± 5 turns	∞
τ_{max}	70 Nm	20 Nm

Table 3.2: Mechanical overview of both identified joints

Chapter 4

Modelling and Compensation of Non-Idealities

This chapter discusses, for each part individually, different non-idealities, as they occur in flexible robotic joints. Some of them are more severe than others, so that some of them will be regarded more closely.

4.1 Rotary Encoder

In use for joint A and for several further joint designs is a rotary encoder that works according to the magnetic principle as described in Sec. 2.1.1.4. The product is said to be capable of 18 bit resolution, but only with applied filter terms. It provides a wide range of noise reduction filters, but most of them come with an additional delay for calculation. The filter with 27 dB noise reduction will be used, since it is the best filter with constant delay time.

4.1.1 The Rotary Encoder Test Bench

For this identification setup, an extra test bench (Fig. 4.1) has been built. It simply consists of a BLDC motor (for automatic movement), a reference sensor (S1) and the sensor to be identified (S2). To guarantee exact (and precisely changeable) alignments of the sensor S2, it is mounted on a 6-axis micro-movement stage by *ULTRAlign*. To compare the two sensors, it is necessary to know the mechanical position of the two sensors. As they have not been mechanically aligned, this has to be done mathematically via an offset value. This offset can be calculated on a static measurement of multiple positions over long time. To compensate possible direction-dependent offsets, the motor was rotated clockwise and counter-clockwise. Because S1 has a 3 bit higher resolution than S2 (Tab. 4.1), the results have to be multiplied with $2^4 = 16$ to be comparable. The mechanical

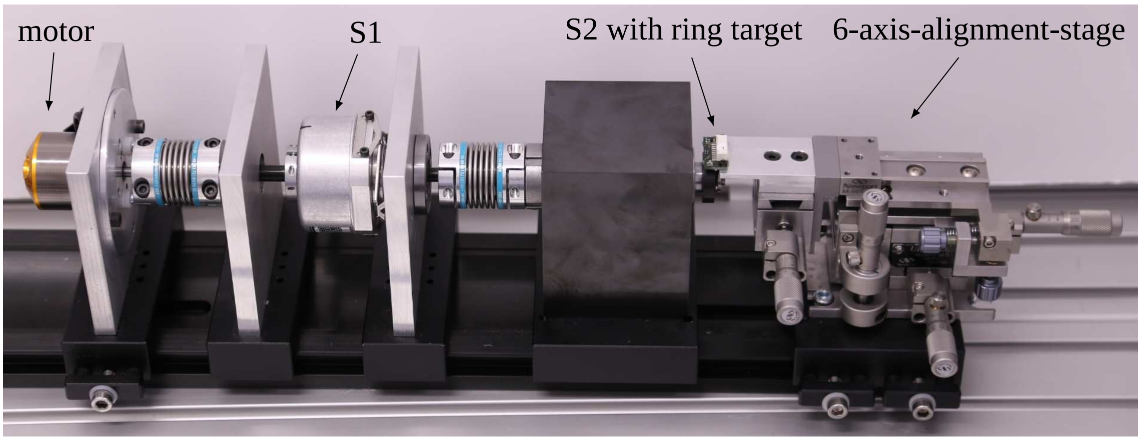
motor
S1
S2 with ring target
6-axis-alignment-stage

Figure 4.1: Picture of the rotary encoder test bench

	S1	S2
usage	reference	identification object
theoretical maximal resolution	14 bit	18 bit
communication	QEP	QEP, SPI
working principle	optical	magnetic
targets	integrated	ring (two sizes), disk
max speed	12000 rpm	12000 rpm

Table 4.1: Comparison of both rotation encoders

offset ξ is calculated as the mean value of all position-depending offsets,

$$\xi = \frac{1}{n}\sum_{n} 16x_{S1} - x_{S2}. \tag{4.1}$$

Since single turn sensors are used, an arithmetic mean may result in false results, if the measurement exceeds one complete rotation or contains values near x_0. By interpreting the top half range as negative values, a symmetrical scale is created. The general mathematical procedure for a example value n and the range k would be

$$n_{aligned} = ((n + \frac{k}{2}) \bmod k) - \frac{k}{2} \tag{4.2}$$

With the target resolution of 18 bit resulting in 2^{18} points per rotation, the offset alignment calculation looks as follows

$$\xi = \frac{1}{n}\sum_{n}(((16x_{S1} - x_{S2} + 2^{17}) \bmod 2^{18}) - 2^{17}) \tag{4.3}$$

In the used setup, the resulting offset value is 109437.

4.1.2 Time Behavior of the Encoder

As depicted in Fig. 4.2 and Fig. 4.3, on top of the position dependent shape comes an independent and very high offset. A test run reveals, that this offset is velocity dependent: Delayed by calculations and filtering, S2 provides its signals much later than the reference sensor (S1).

desired speed	[rpm]	-1500	-1000	-500	500	1000	1500
real speed (average)	[rpm]	-1483	-992	-499	497	990	1478
disparity	[points]	404	271	137	144	285	424
error per speed	[points/rpm]	0.2724	0.2735	0.2748	0.2904	0.2887	0.2869

Table 4.2: Disparity caused by time difference

The relative disparity (absolute error per resolution) equals the product of speed and time. With an average disparity (see Tab. 4.2) of 0.2811 points per rpm,

$$\frac{0.2811}{2^{18}} = \frac{\text{rpm}}{60\ \text{s}}\Delta t, \tag{4.4}$$

the delay can be calculated to

$$\Delta t = 64.34\ \mu s. \tag{4.5}$$

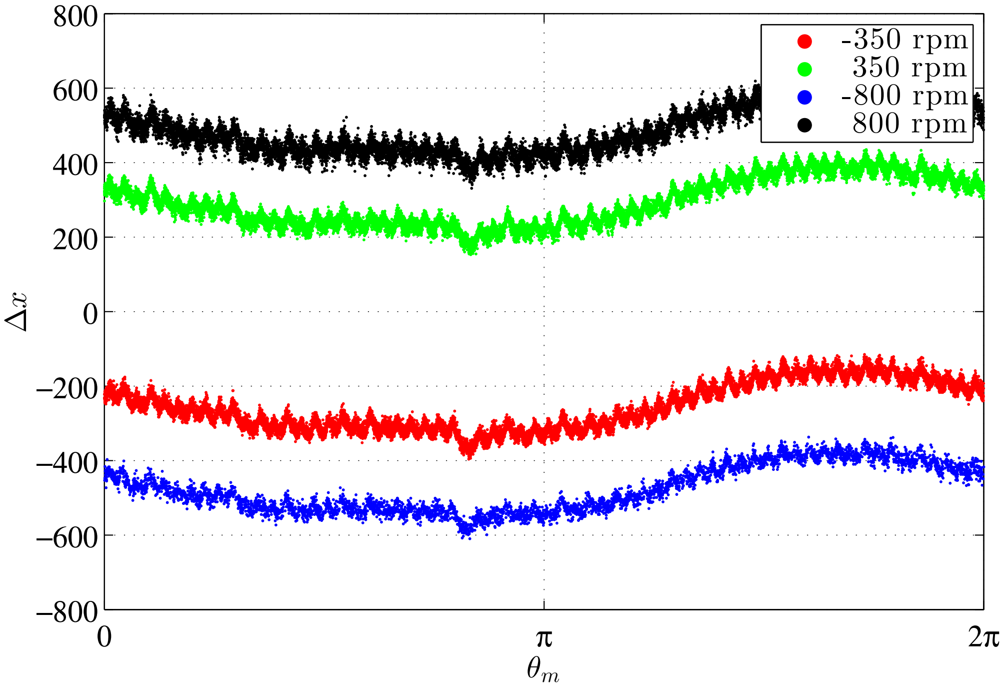

Figure 4.2: Velocity dependent shift

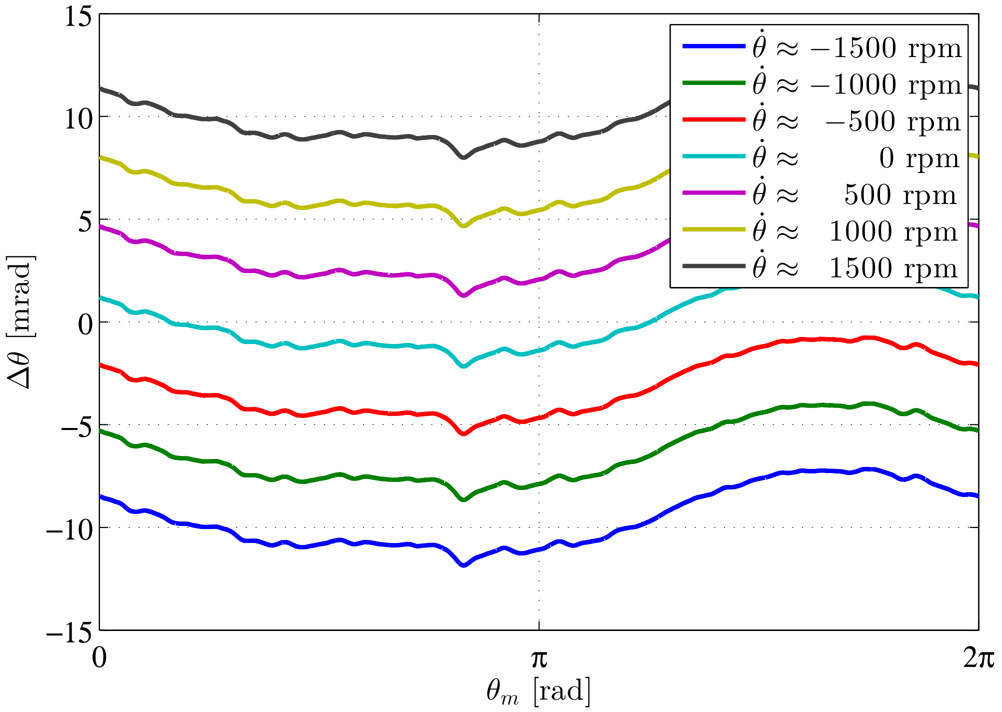

Figure 4.3: Velocity dependent shifts in comparison (filtered)

desired speed	[rpm]	-1500	-1000	-500	500	1000	1500
real speed (average)	[rpm]	-1483	-992	-499	497	990	1478
expected filter ($10\ \mu s$) shift	[points]	64.8	43.4	21.8	-21.7	-43.3	-64.6
real shift	[points]	70.9	48.2	23.3	-24.6	-47.7	-70.0
missing delay	[μs]	0.94	1.11	0.69	1.34	1.02	0.84

Table 4.3: Disparity caused by filter runtime

Filtering the measurement by 27 dB, the datasheet states a delay of $10\ \mu s$. Since this would generally apply to all results, this causes a velocity dependent shift, but not the splitting. This delay causes a shift of

$$\frac{\Delta x}{\text{rpm}} = \frac{2^{18}}{60\ \text{s}}\Delta t, \tag{4.6}$$

$$\Delta x = \frac{0.0437}{\text{rpm}}. \tag{4.7}$$

As it can be seen in Tab. 4.3, those $10\mu s$ cover most of the occurring delay. The additional (fluctuate) delay of circa $1\mu s$ can be explained by the changing delay between the sensor readouts caused by interrupt routines for speed control and sampling interferences.

4.1.3 Linearity of the Sensor

For reliable measurements, the sensor will be surveyed. This is done by a step-to-step comparison to the reference sensor (S1, see Tab. 4.1). Several issues may occur, such as a sinusoidal error („beat“) based on possibly mechanical misalignment of the particular encoder axis. Furthermore, it is possible, that systematic and manufacturing errors such as non-linear gradients or unrecognisable areas appear. In the used setup, several effects are visible. The error shape (Fig. 4.4) shows a high amplitude beat, and additional repeating side effects. This effects and their possibility of compensation will be identified and discussed in Sec. 4.1.5.

4.1.4 Positioning of the Decoder Chip

Important for production planning is the mechanical tolerance of the used parts. False positioning may falsify the measurement results and may therefore cause further damage to the mechanics and the environment. With the rotary encoder test bench (see Sec. 4.1.1), it is possible to precisely place the decoder integrated circuit (IC) in relation to the target to evaluate the impacts of misplacement.

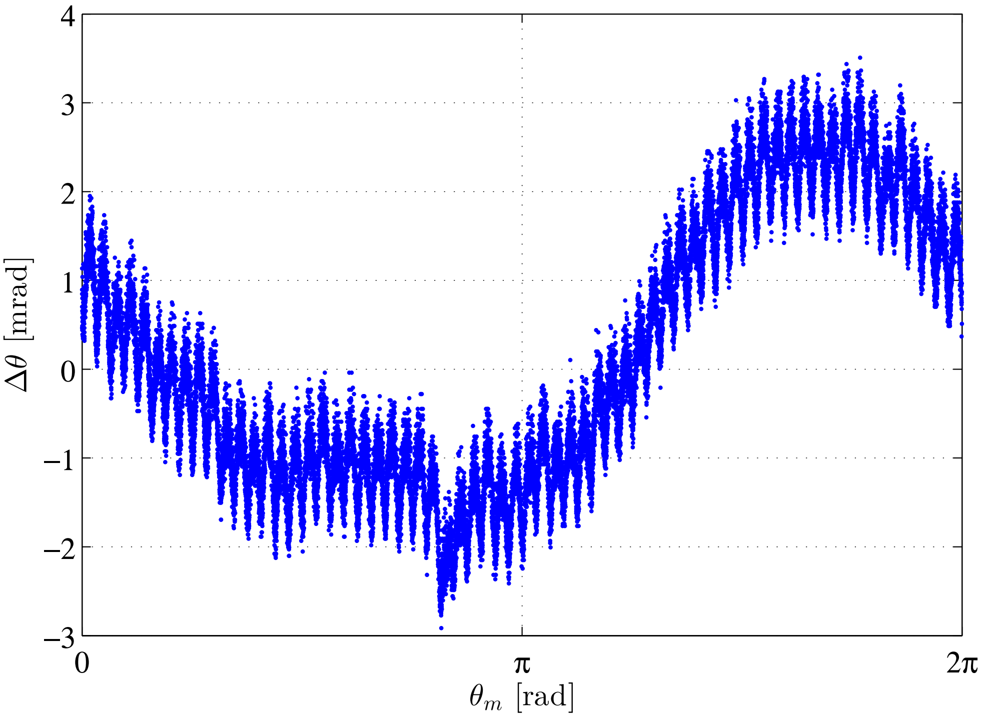

Figure 4.4: Error shape S2 vs. S1

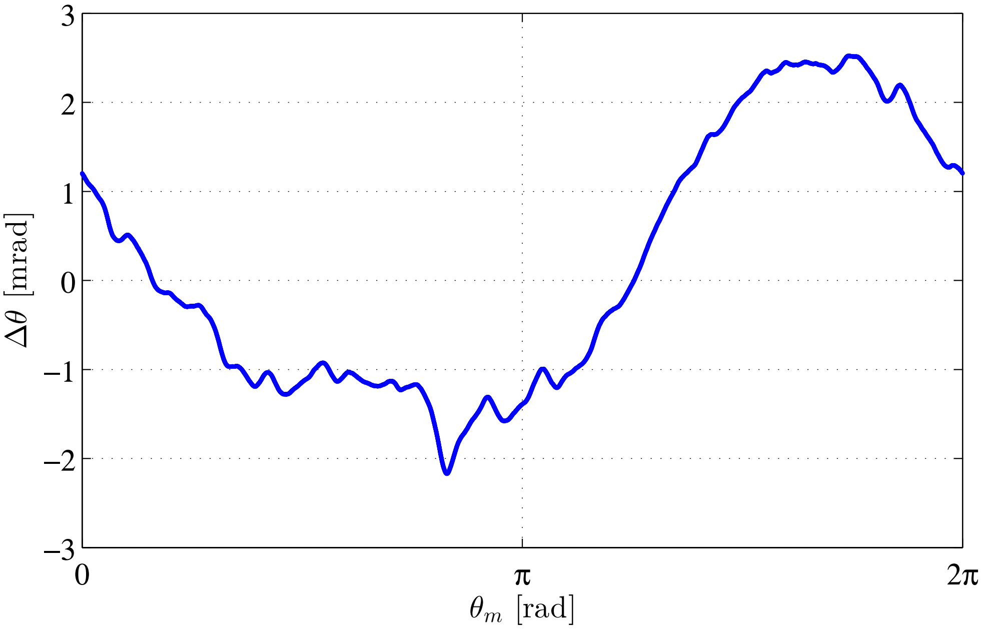

Figure 4.5: Smoothed error shape S2 vs. S1 used for compensation

direction	estimated manufacturing tolerance	tested tolerance	period counter consistency error at	unit
radial shift	±0.15	±0.2	-0.25 / $+0.3$	mm
axial shift	±0.15	±0.25	±0.65	mm
rotation of sensor chip	±0.5	±0.7	±1.0	°
axial tilt of sensor chip	±0.5	±0.1	±1.5	°
vertical shift	±0.5	±1.0		mm

Table 4.4: Measured positions

The measurements show, that as long as positioned in range Tab. 4.4, the misalignment has no mayor influences on calculation and precision. If the tolerances are exceeded, the sensor returns an error titled as ’period consistency error’, that means in effect that the position could not be calculated correctly.

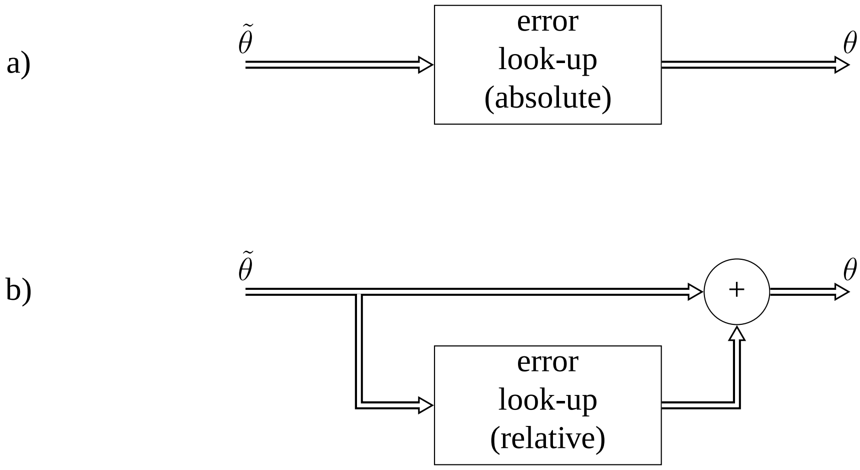

Figure 4.6: Schematic of position error compensation: a) direct compensation; b) compensation via error

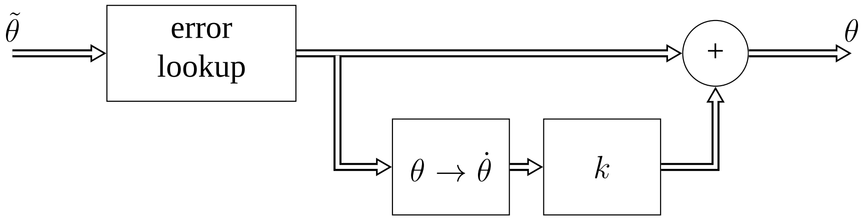

Figure 4.7: Schematic of position error compensation with velocity consideration

4.1.5 Compensation

Two possibilities of feed-forward compensation are visualized in Fig. 4.6. Practically, they are equivalent, but dependent on the calculation speed, one may be preferable. In the given setup, the direct lookup-table is used. The table contains a negotiated version of the smoothed error plot (Fig. 4.5) as shape correction. The amplitude of the shape correction is about 250 points, therefore the usable precision over all would decrease with factor 256 (8 bit). This would reduce the resulting precision (ignoring noise effects) down from 18 bit to 10 bit.

For the correction, the smoothed and noise-reduced curve of Fig. 4.5 will be used. Due to storage space restrictions, the span of all 2^{18} possible positions will be reduced to 2^{14} values. The mean error at this is less then 1 bit over all. Note, that an error of 1 can never be detected precisely, as the offset calculation does not allow such precise results. Fig. 4.8 and Fig. 4.9 show the impact of the applied compensation. The available precision rises up to 14 bit. The enhanced precision can also be verified by the histograms Fig. 4.10 and Fig. 4.11. To compensate the speed dependent offset caused by the filter delay (Sec. 4.1.2), an additional velocity-dependent term would be imaginable. Its structure is visualized in Fig. 4.7.

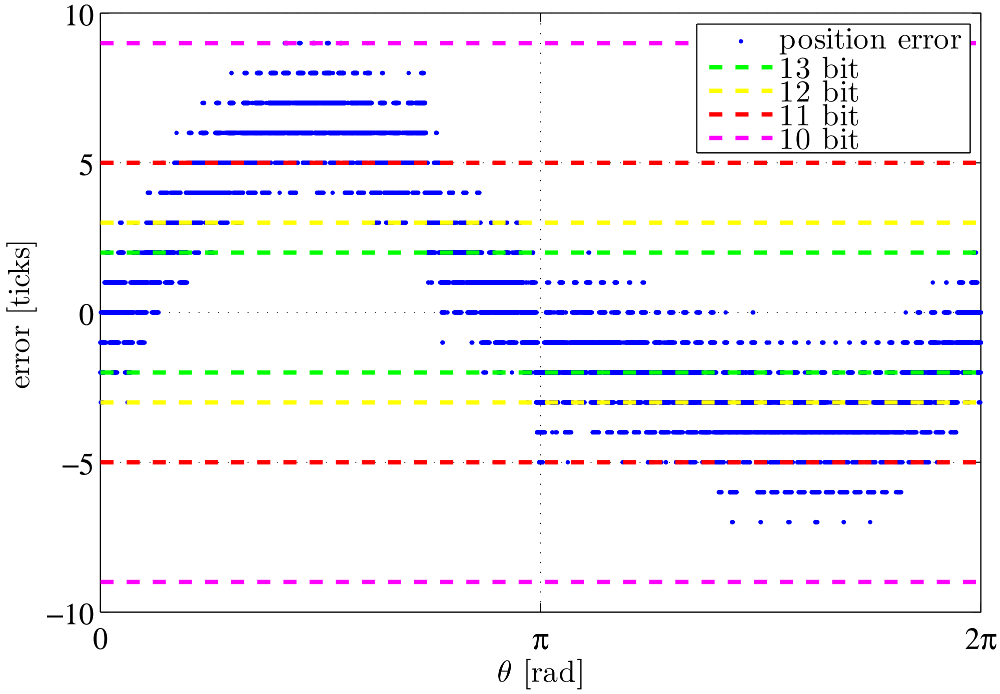

Figure 4.8: Error distribution over one revolution

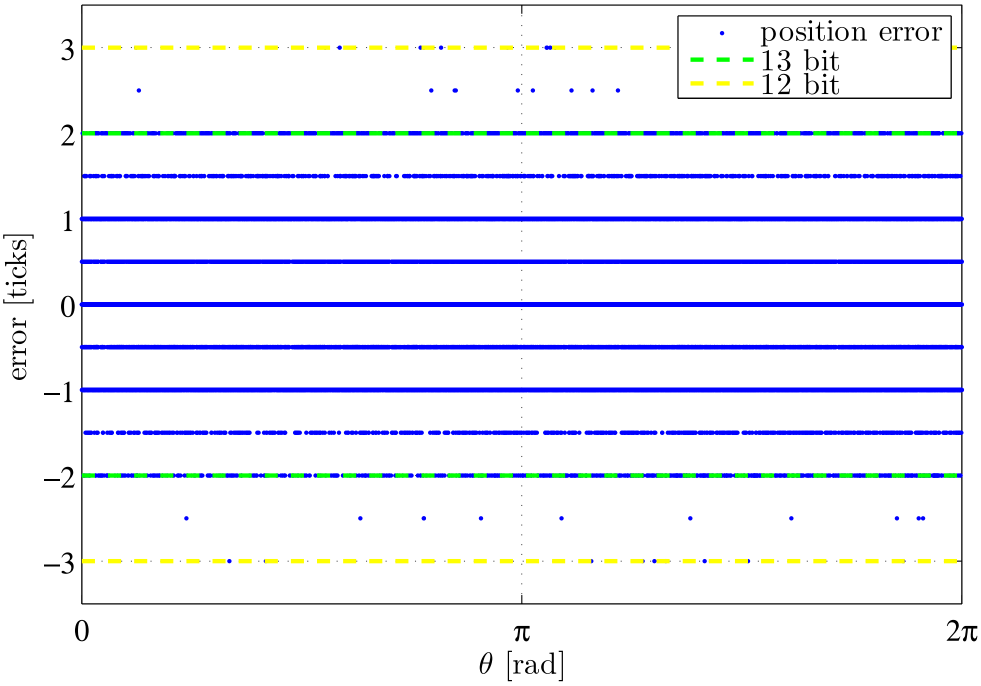

Figure 4.9: Error distribution over one revolution with applied shape correction

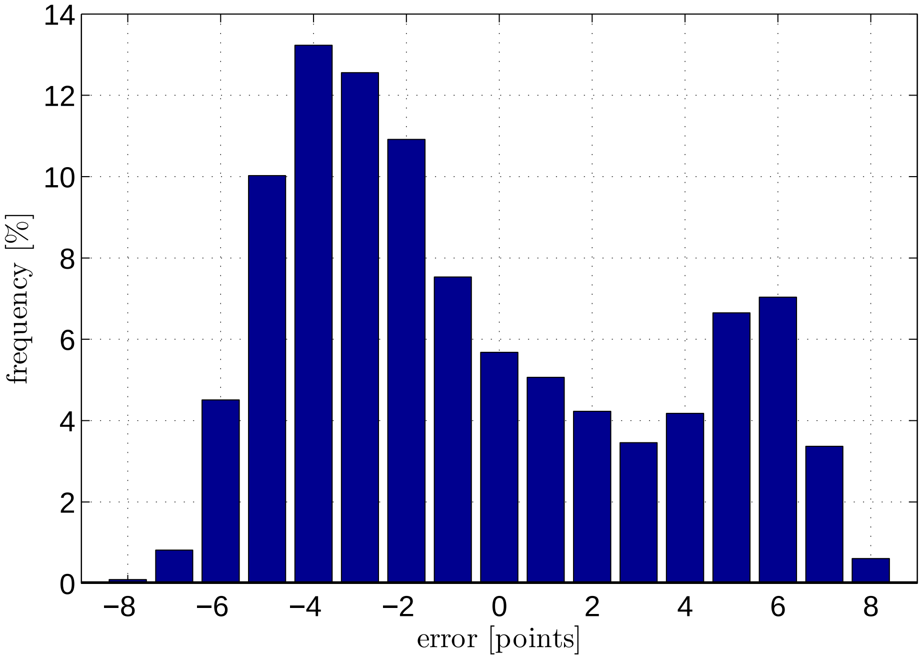

Figure 4.10: Histogram: Error distribution

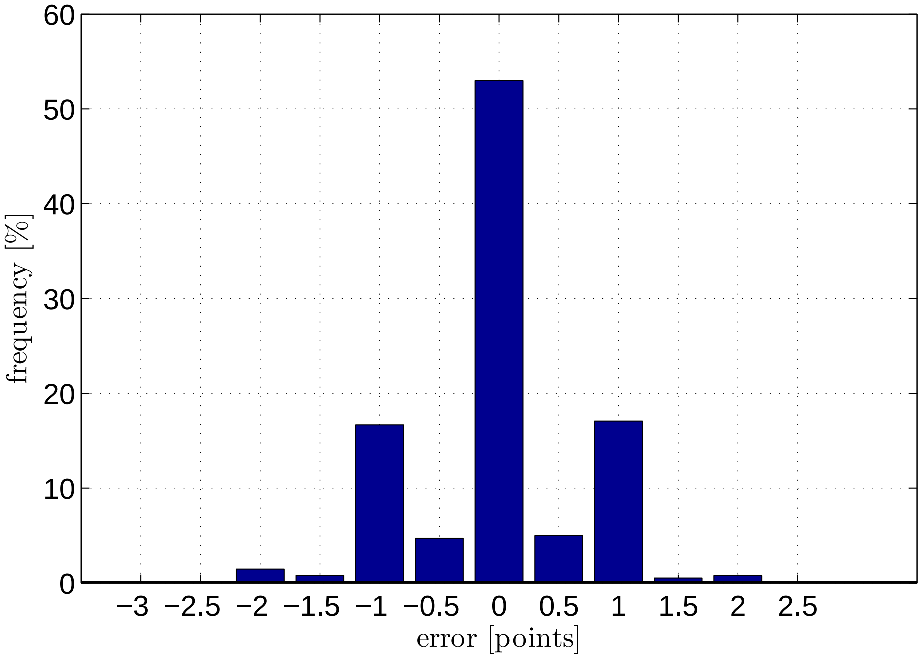

Figure 4.11: Histogram: Error distribution over one revolution with applied shape correction

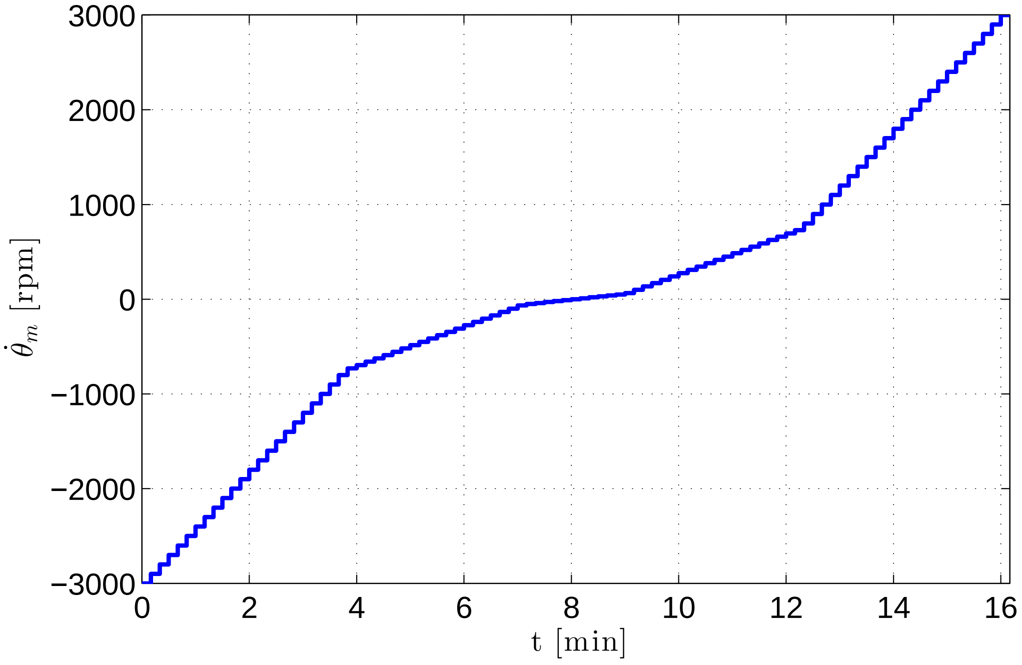

Figure 4.12: Speed profile used for static friction identification

4.2 Friction Modelling and Identification

4.2.1 Measuring Static Friction

To measure the friction, the following measurement method turned out to be the most reliable. The joint is running freely without load for an specified velocity profile. This Profile can be seen in Fig. 4.12. The number of individual measurements around $\dot{\theta} \approx 0$ increases, as the most interesting parameters are identified there. The friction itself is calculated via the motor current and the according motor constant k_m as

$$\tau_m = k_m i_q. \tag{4.8}$$

Thereby, i_q resembles the d/q-transformed direct motor current. Continuously changing velocity would generate more homogeneous results, but for noise reduction, a period of constant velocity is required. Unfortunately, the signal-to-noise ratio (SNR) is very low in this system, so the noise reduction takes a large amount of readings.
The Figures 4.13 and 4.14 each show the friction over velocity, that has been measured. This values are used to parametrize the static friction models.

4.2.2 Coulomb and Viscous Friction

The previously mentioned coulomb friction model (see Sec. 2.3.1.1) is the most basic friction model as it assumes τ_f to be constant over all velocities. This behaviour is very

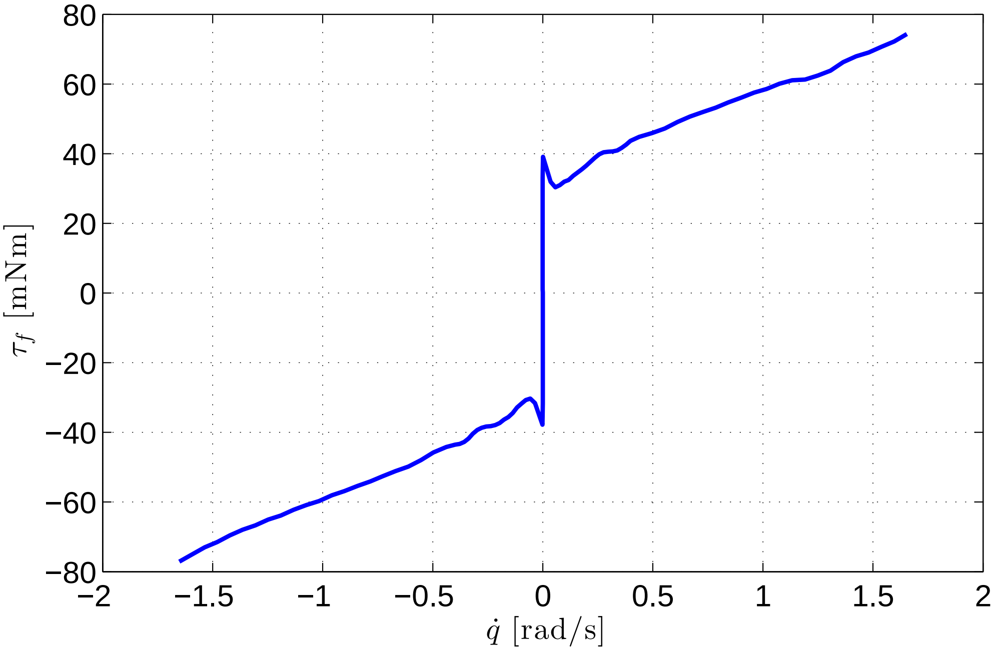

Figure 4.13: Static friction curve of joint A

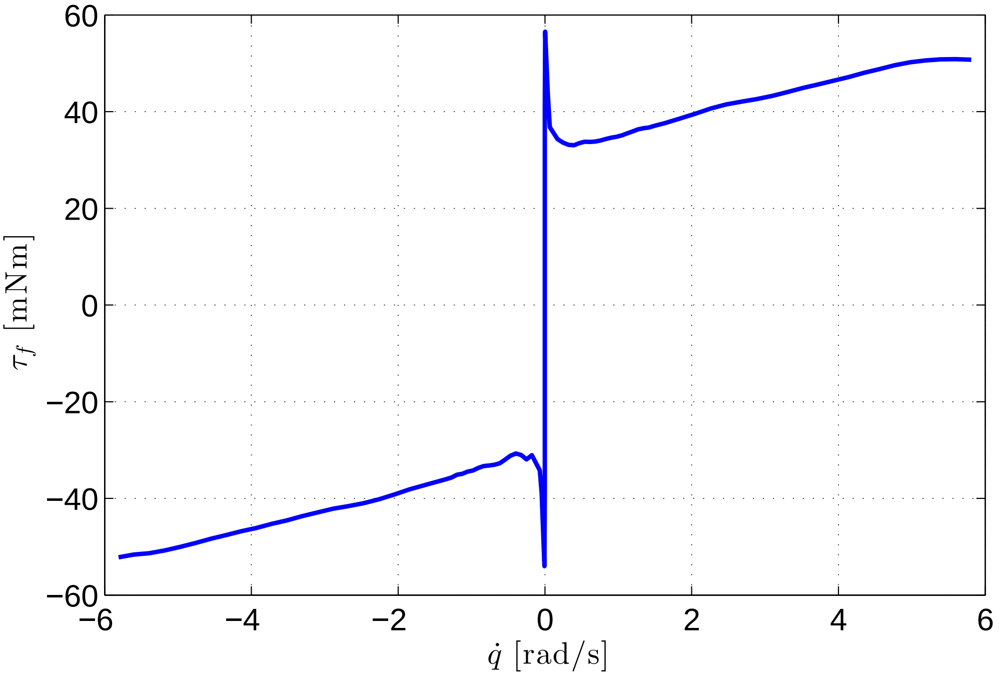

Figure 4.14: Static friction curve of joint B

parameter	joint A (3.2)	joint B (belt)	unit
τ_c	0.030	0.031	[Nm]
c_v	$1.583 \cdot 10^{-5}$	$8.205 \cdot 10^{-6}$	$[\frac{\text{Nm}}{\text{rpm}}]$
c_v	$1.512 \cdot 10^{-4}$	$7.835 \cdot 10^{-5}$	$[\frac{\text{Nm s}}{\text{rad}}]$

Table 4.5: Fitted model parameters for the coulomb and viscous friction friction models

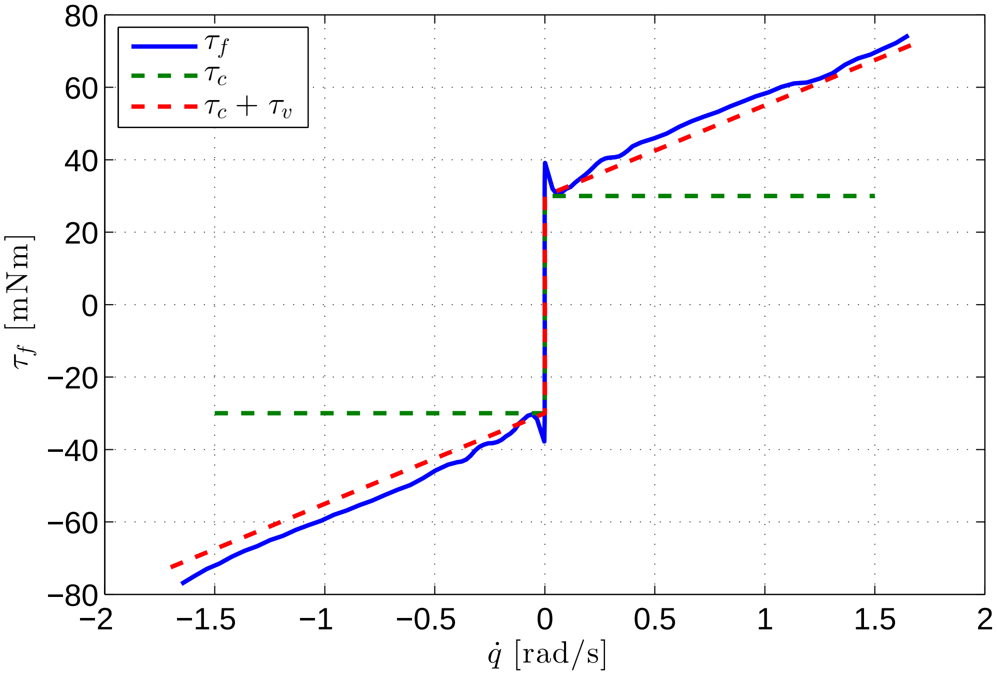

Figure 4.15: Measured friction with coulomb and viscous friction modelled for joint A

easy to implement as compensation but not yet very detailed. A better way is the viscous model (see Sec. 2.3.1.3) as it is linear velocity dependent and shows deviation in slow velocities.

4.2.2.1 Model Parameterization

With the measured values from Sec. 4.2.1, Tab. 4.5 contains the isolated parameters for the coulomb and the viscous friction models. The result of modelling with either only coulomb friction, or coulomb and viscous friction can be seen in Fig. 4.15 respectively Fig. 4.16. Note that it is very important, that the friction is never **over**compensated, because that would lead to an active controller behaviour.

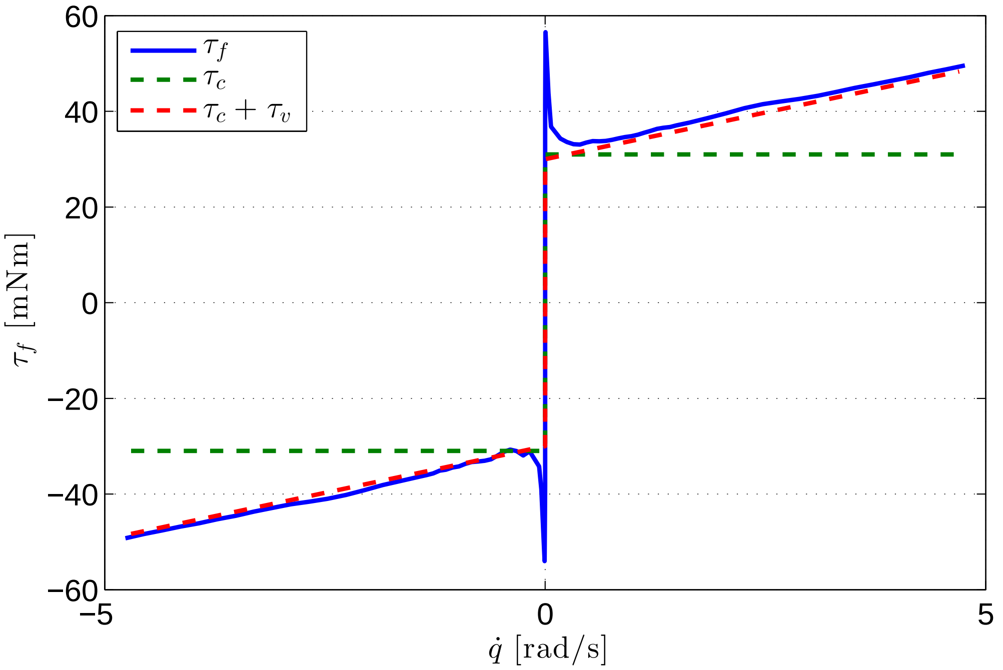

Figure 4.16: Measured friction with coulomb and viscous friction modelled for joint B

4.2.2.2 Model Verification

To verify the correct modelling, both friction models have been ported to the joint controlling DSP. They are implemented as look-up table against $\dot{\theta}$. According to the feedforward method, the estimated friction torque is added to the controlled current i_q.

4.2.3 Complete Static Friction Model

Extending the friction model by the Stribeck effect (see Sec. 2.3.1.5) and thus with stiction modelling (see Sec. 2.3.1.4), the parametrization is shown in Tab. 4.6. The results are depicted in Fig. 4.17 and Fig. 4.18.

4.2.4 Compensation with Static Friction Models

The compensation performance is measured in control accuracy either as sum of errors or sum of square-errors,

$$p_{1,total} = \sum |\theta_d - \theta| \tag{4.9}$$

and

$$p_{2,total} = \sqrt{\sum (\theta_d - \theta)^2}. \tag{4.10}$$

The maximal positioning error is noted as p_{max}.

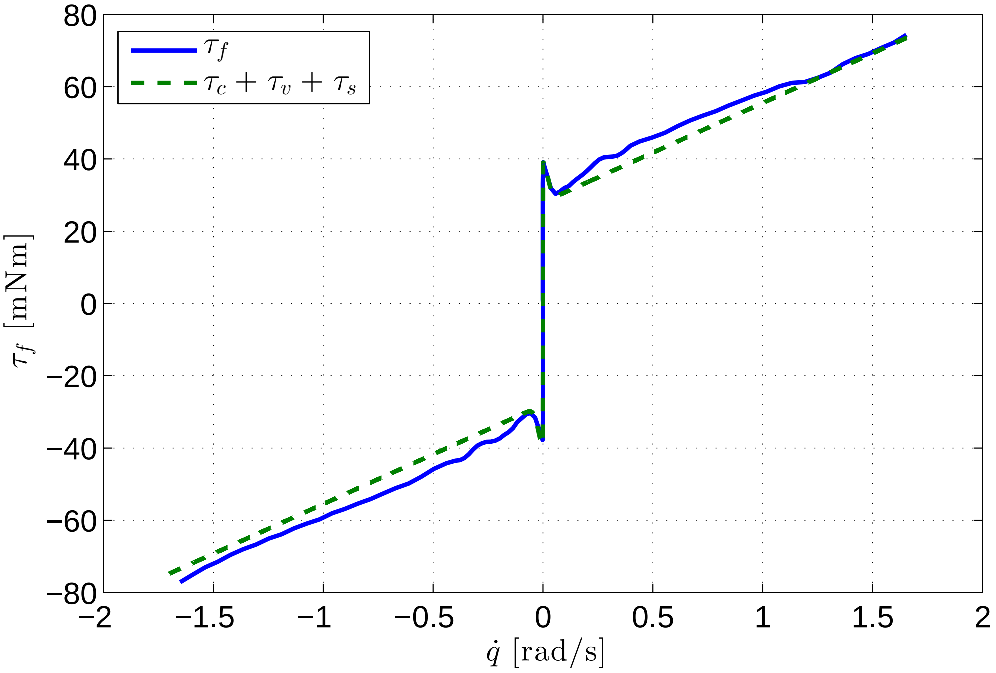

Figure 4.17: Measured friction with complete static friction model for joint A

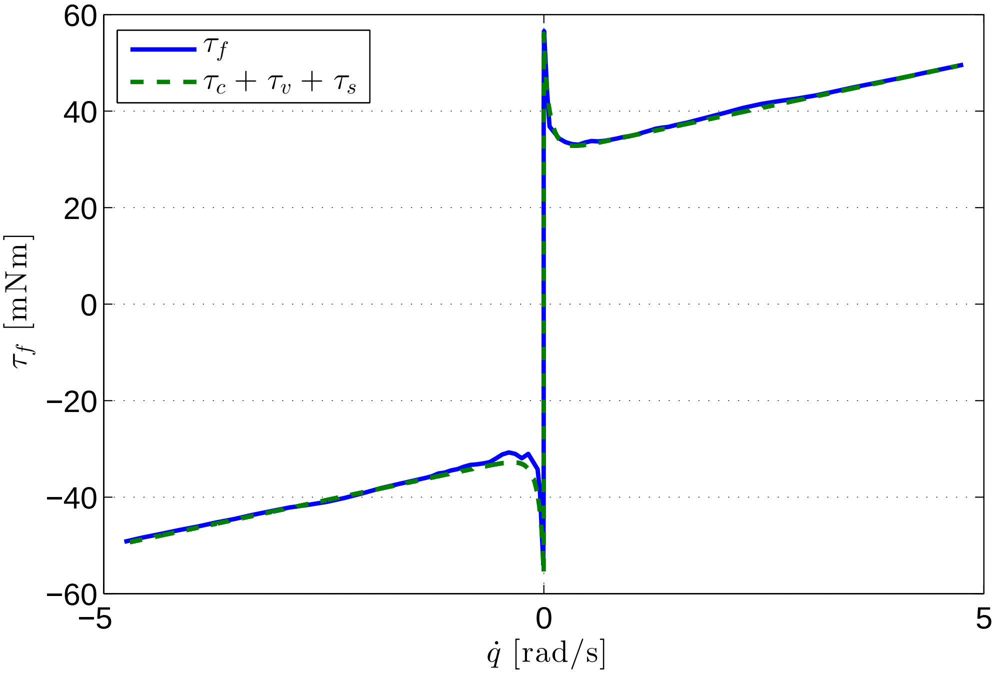

Figure 4.18: Measured friction with complete static friction model for joint B

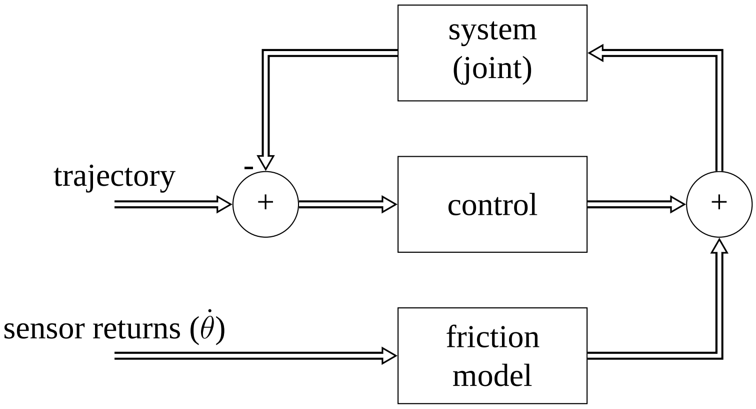
system
(joint)
trajectory
-
+
control
+
sensor returns ($\dot{\theta}$)
friction
model

Figure 4.19: Schematic of the implemented friction compensation structure

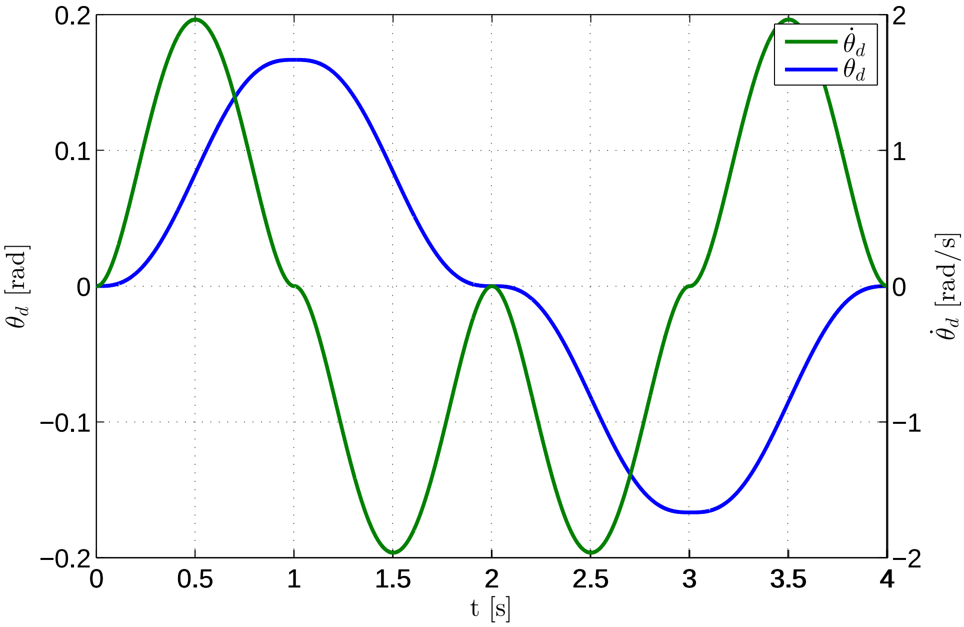

Figure 4.20: Position and speed profile for compensation evaluation

parameter	joint A (3.2)	joint B (belt)	unit
τ_c	0.030	0.031	[Nm]
τ_h	0.039	0.057	[Nm]
c_v	$1.583 \cdot 10^{-5}$	$8.205 \cdot 10^{-6}$	$[\frac{\text{Nm}}{\text{rpm}}]$
c_v	$1.512 \cdot 10^{-4}$	$7.835 \cdot 10^{-5}$	$[\frac{\text{Nm s}}{\text{rad}}]$
$\dot{\theta}_s$	0.06	0.08	[rad/s]
δ_s	0.8	1.9	[1]

Table 4.6: Fitted model parameters for the complete static friction model

4.2.4.1 Coulomb Friction Model

As it can be seen in Fig. 4.22 a), the coulomb friction model has a high leap around $\dot{\theta} \approx 0$. This causes most controllers to become unstable under several circumstances. Especially in position control mode, this can be a big problem towards small movements and precise positioning as it supports oscillations. The simplest avoidance is the introduction of a non-compensation-area with possibly small width around zero (Fig. 4.22 b). Since this solution provides additional leaps, a linear rising bypass has been implemented (Fig. 4.22 c). This method provides a completely leap-less shape, therefore allows smoother controlling. The best results have been achieved with a threshold speed $\dot{\theta}_{m,t}$ of ± 0.05 rad/s. Interestingly, the controller performance sometimes is better with model (b) than with model (a) or (c) and even better than in combination with viscous friction. Nevertheless, this concept produces several overshoots and additional permanent errors as it can be seen in Fig. 4.23.

4.2.4.2 Coulomb and Viscous Friction Model

The same procedure is applied with the combined models of coulomb and viscous friction. Again, the area around $\dot{\theta} \approx 0$ is interpolated as linear (Compare Fig. 4.24 a) and 4.24 b). As it can be seen in Fig. 4.25, the additional viscous friction model diminishes the deviation in higher speed regions. Still, several overshoots and imprecisions can be found in slow velocities.

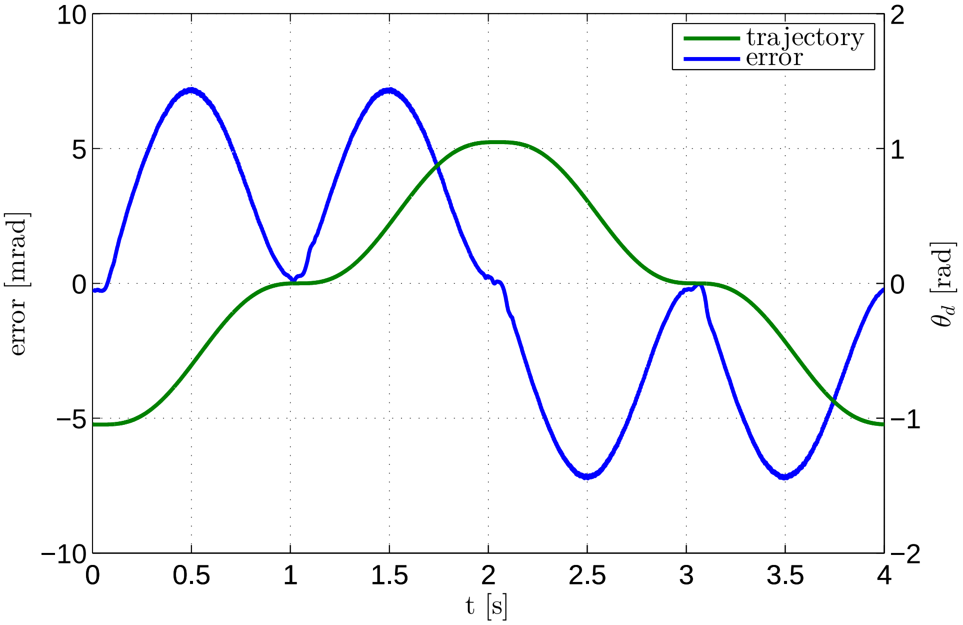

Figure 4.21: Reference trajectory for comparison (without any friction compensation) [joint A]

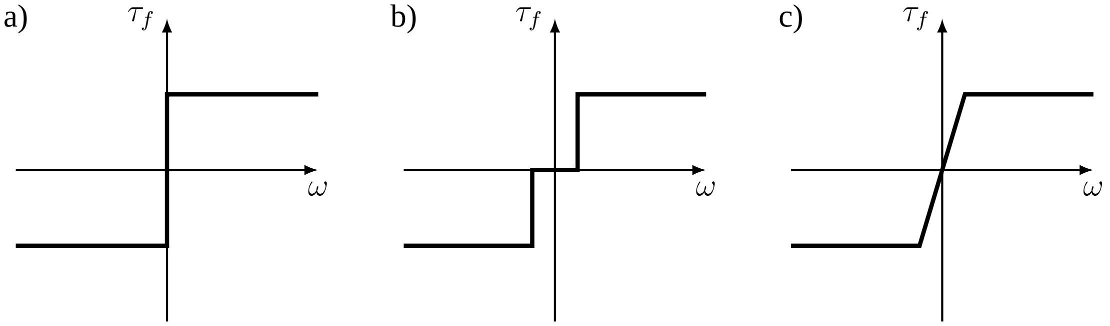
a)
τ_f
ω
b)
τ_f
ω
c)
τ_f
ω

Figure 4.22: Ideal coulomb friction model (a); with simple avoidance of the critical discontinuation (b); and leap-less model adaptation (c)

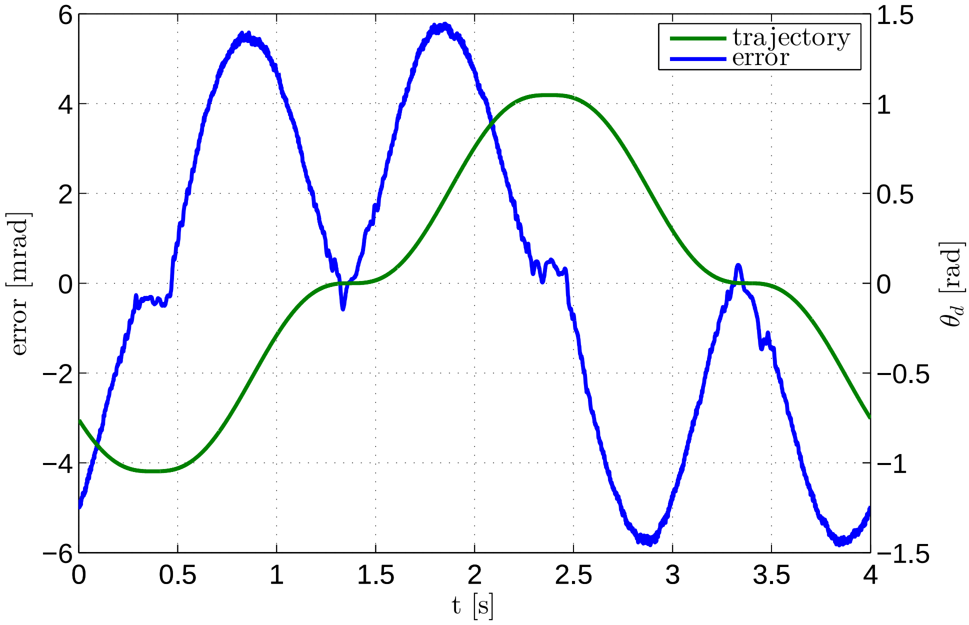

Figure 4.23: Friction compensation with coulomb friction model (c)

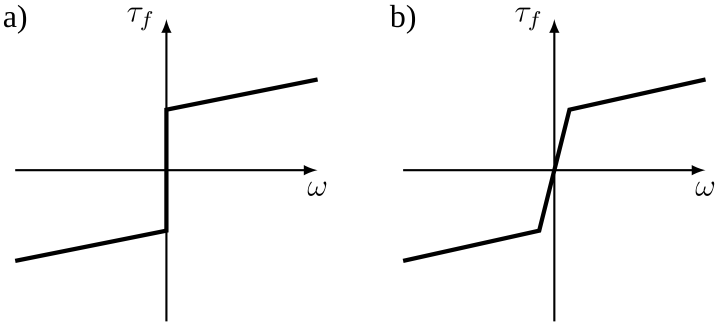
a)
τ_f
ω
b)
τ_f
ω

Figure 4.24: Ideal friction model with coulomb and viscous friction (a) and leap-less model adaptation (b)

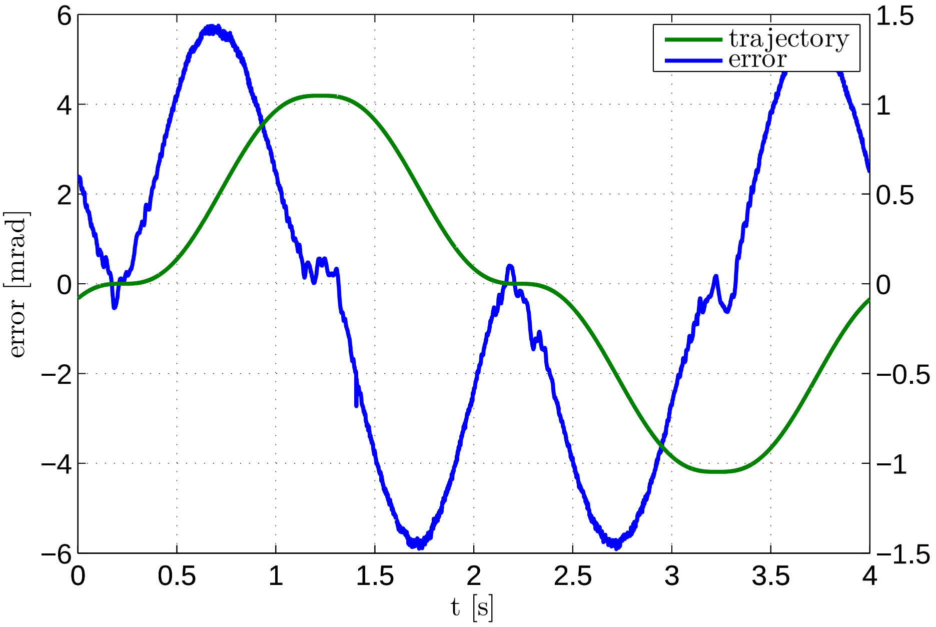

Figure 4.25: Friction compensation with coulomb-and-viscous friction model (b)

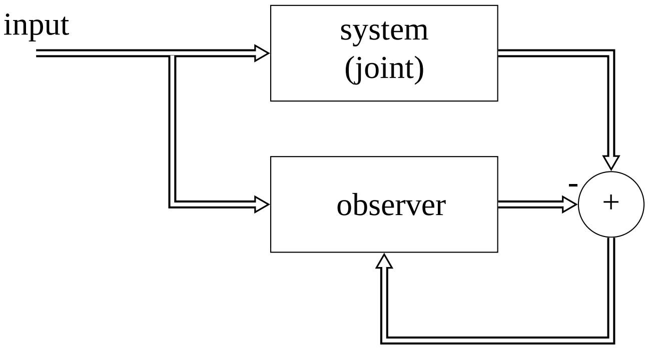

Figure 4.26: Observer control structure

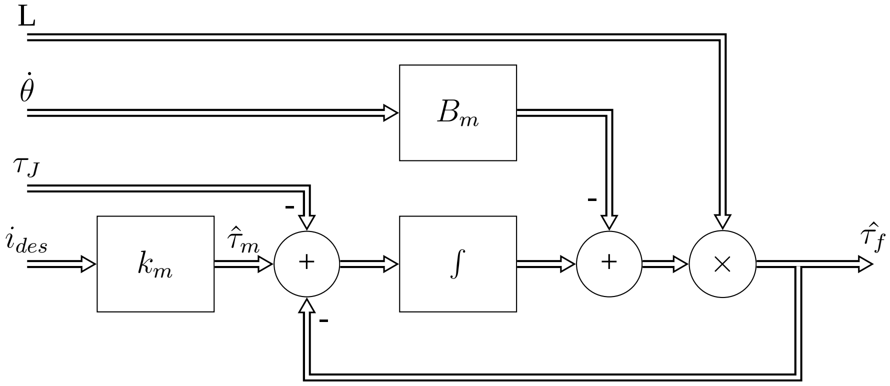

Figure 4.27: Friction observer schematic

4.2.4.3 Complete Static Friction Model

The advantaged of the complete static friction model (with Stribeck effect and Stiction) over the combined coulomb and viscous friction model are located in a small area around $\dot{\theta} \approx 0$. With the need and implementation of the zero-substitution, all advantages of the complete model over the combined coulomb and viscous models would be void. This means, the adapted model would be exactly the same as the interpolated viscous model as presented in Fig. 4.24 b). Therefore, this verification has not been implemented.

4.2.5 Compensation with Friction Observer

In control theory, They estimate the systems' responses and react to differences between calculated response and real response. More about the working principle and appliances can be found in [41] and [42]. In usage is a very basic observer, that compares the estimated overall torque (calculated out of the motor current) with the measured joint torque τ_J. The difference is assumed to be friction or rather the current torque value for the present friction. The schematic can be seen in Fig. 4.27.

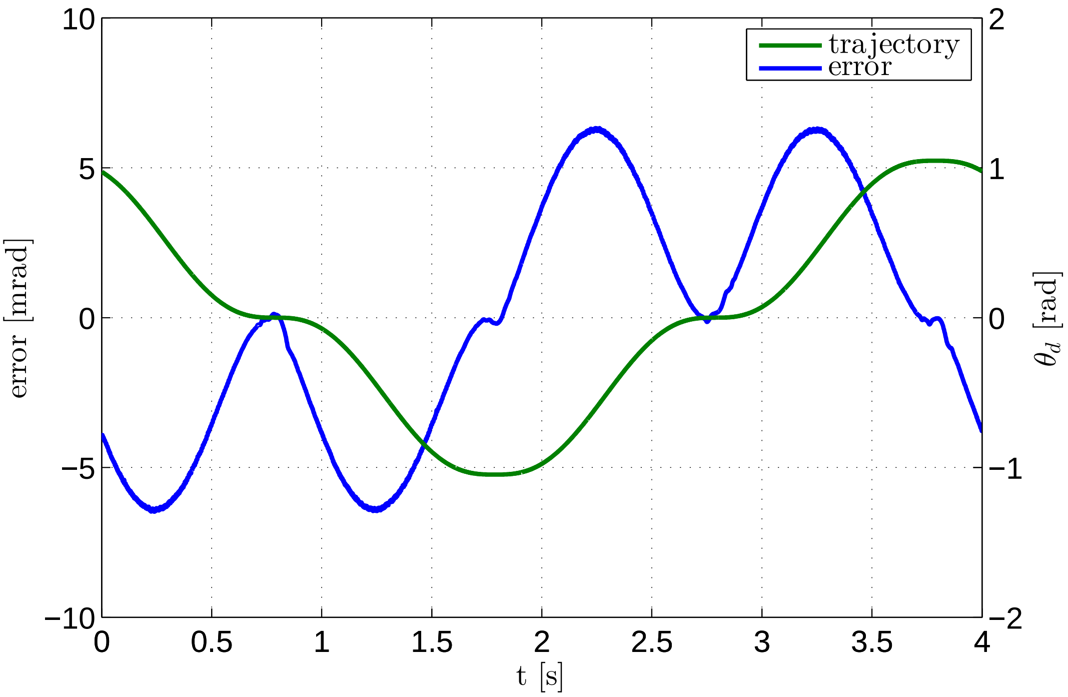

Figure 4.28: Control error with friction observer compensation

4.2.6 Comparison

An overview of all evaluated compensation methods and models is shown in Tab. 4.7. The analysed methods show a decrease of the overall position error, but in crucial areas ($\dot{\theta} \approx 0$), the observer is the only structure, that does not create overshoots. It also has the highest precision enhancement rates as well as the least maximum error p_{max}. Therefore, it clearly is the best strategy that has been evaluated. Further improvements may be produced with either different friction models (dynamic as well as completely different approaches), or a possible combination of both friction modelling and observing.

model	error	joint A	joint B
none (reference)	p_1	$3.948 \cdot 10^{-3}$	$3.904 \cdot 10^{-3}$
	p_2	$7.640 \cdot 10^{-1}$	$6.935 \cdot 10^{-1}$
	p_{max}	$7.640 \cdot 10^{-3}$	$7.245 \cdot 10^{-3}$
coulomb with zero-area	p_1	$3.428 \cdot 10^{-3}$	$3.098 \cdot 10^{-3}$
	p_2	$5.620 \cdot 10^{-1}$	$5.690 \cdot 10^{-1}$
	p_{max}	$7.519 \cdot 10^{-3}$	$7.844 \cdot 10^{-3}$
coulomb interpolated	p_1	$3.398 \cdot 10^{-3}$	$3.215 \cdot 10^{-3}$
	p_2	$6.732 \cdot 10^{-1}$	$6.256 \cdot 10^{-1}$
	p_{max}	$6.557 \cdot 10^{-3}$	$7.653 \cdot 10^{-3}$
coulomb-and-viscous	p_1	$3.417 \cdot 10^{-3}$	$3.071 \cdot 10^{-3}$
	p_2	$6.766 \cdot 10^{-1}$	$5.984 \cdot 10^{-1}$
	p_{max}	$6.606 \cdot 10^{-3}$	$7.688 \cdot 10^{-3}$
observer	p_1	$3.415 \cdot 10^{-3}$	$3.321 \cdot 10^{-3}$
	p_2	$6.685 \cdot 10^{-1}$	$6.310 \cdot 10^{-1}$
	p_{max}	$6.480 \cdot 10^{-3}$	$6.400 \cdot 10^{-3}$

Table 4.7: Overview of positioning precision with different friction compensation methods (all numbers given in [rad]); less is better

4.3 Joint Flexibility

For the production of lightweight joints, materials with high strength per weight are required. Based on this, most mechanical elements show a high amount of flexibility. The two main causes inside the joint are the torque sensor and the SWG, more precisely its flex spline. Since there is no compromise between sufficiently stiff solutions and reduced weight, the flexibility is commonly accepted and taken into consideration. The commonly used method is presented in [43], [44] and [29] among others. It suggests the stiffness to be a linear factor (or in multidimensional systems a matrix) to the measurable bending,

$$\tau = k(q_i - q_j). \tag{4.11}$$

For one single joint with just one actuator, the equation simplifies to

$$\tau = k(q - \theta), \tag{4.12}$$

$$\Delta\tau = k\Delta q, \tag{4.13}$$

the difference between measured motor position and measured link position. An ideal joint without flexibility ($q = \theta$) would have the stiffness $k = \infty$. With knowledge of the applied torque, it is easy to calculate the actual bending, as long as it can be modelled as an ideal spring,

$$\Delta x = k^1 f, \tag{4.14}$$

$$\Delta\theta = k^1 \tau. \tag{4.15}$$

For most structural parts and joint parts this assumption is valid.

4.3.1 Measurement Method

To identify the flexibility parameter (stiffness) K, the joints (mounted on the joint test bench Sec. 3.2) are powered with varying load at constant speeds. Thereby, the torsion will be measured via the difference of the motor-encoder and an external position encoder at link, as it provides a higher resolution than the internal link sensor. For compensating the mechanical offset and comparing the two position values, the same technique as in Sec. 4.1.1 is used,

$$\Delta\boldsymbol{q} = (q \bmod 2\pi - \xi - (\frac{\theta_m}{\beta_{tr}} \bmod 2\pi) + \pi) \bmod 2\pi - \pi, \tag{4.16}$$

with β_{tr} as the joints transmission ratio and ξ as the mechanical offset between both sensors. As mentioned in Sec. 3.2, the test bench is capable of two ranges of load: 0 to 17 Nm with brake A, and 5 to 150 Nm with transmission and brake B. In this identification process, both ranges were used, depending on the maximum torque the joints can provide. Since joint B is only capable of $\tau_l = 20$ Nm, the second run with brake B has been spared. The test is driven with constant speed in alternating directions, while the load torque τ_l increases. The need for alternating directions arises from the limited spinning ability of joint B (see Tab. 3.2).

4.3.2 Evaluation

The measured $\Delta\theta$ (as seen in Fig. 4.29 and Fig. 4.30) is interpreted as

$$\Delta\theta = k^{-1}\tau + \beta_p \operatorname{sgn}(\tau). \tag{4.17}$$

Since several stiffnesses, that are not part of the joint, are involved in the measurement, the result has to be corrected:

$$k_{total} = \left(\sum \frac{1}{k_i}\right)^{-1} \tag{4.18}$$

$$k_{total} = \left(\frac{1}{k_{joint}} + \frac{1}{k_{bearing}}\right)^{-1} \tag{4.19}$$

$$k_{joint} = \left(\alpha_s - \frac{1}{k_{bearing}}\right)^{-1} \tag{4.20}$$

joint A			
measured	$\tilde{k}^{-1}$	0.1812	mrad/Nm
stiffness bearing	$k_{bearing}$	155.0	kNm/rad
calculated stiffness	k	5.7225	kNm/rad
directional offset	β_o	± 0.5871	mrad

joint B			
measured	$\tilde{k}^{-1}$	1.4746	mrad/Nm
stiffness bearing	$k_{bearing}$	75.0	kNm/rad
calculated stiffness	k	0.6843	kNm/rad
directional offset	β_o	± 0.9588	mrad

Table 4.8: Fitted stiffness parameters for joint flexibility in joint A and joint B

Like the ideal model, joint A provides a linear shape. The torsion is exactly proportional to the applied torque. Similar to Sec. 4.1.2, the directional offset β_o can be explained as the calculation delay of the external position encoder. As a constant value, it doesnt affect the stiffness measurement, that regards only the slope, at all. Unlike joint A, joint B shows a different behaviour. Although it can be assumed linear in the higher load area, it could be fitted differently for the lower torque region. Unfortunately, the used mathematical operators as $\log(\cdot)$ and $\sqrt{\cdot}$, that would be able to approximate the curve are very complex to implement on a DSP. Therefore, there are two resources saving options: assuming the curve to be linear, which will be on expense of precision, or modelling the curve via a

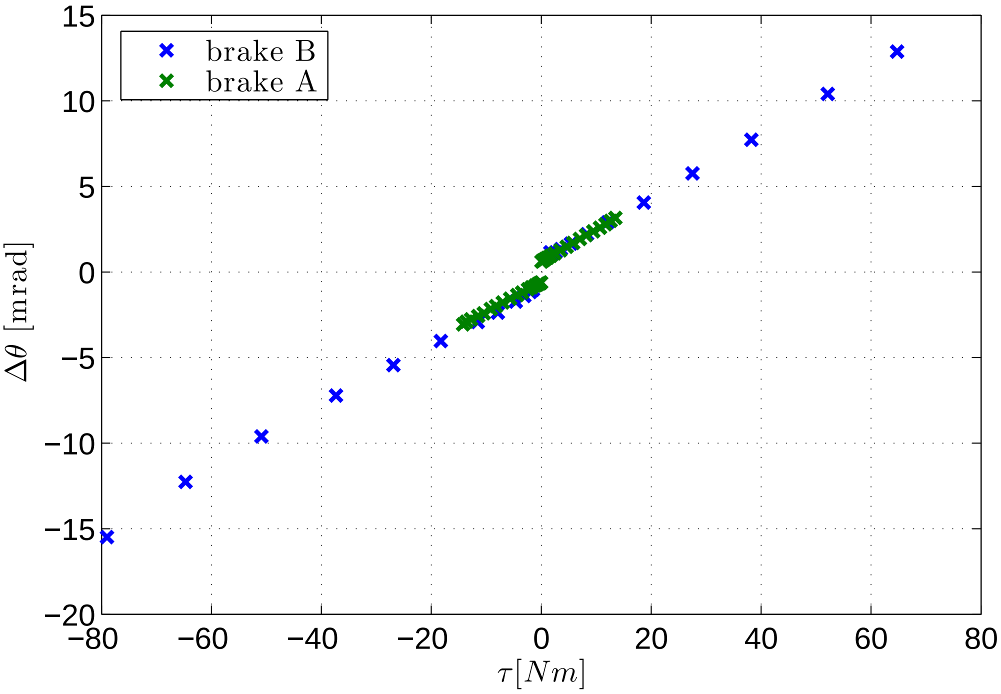

Figure 4.29: Measured joint flexibility in joint A

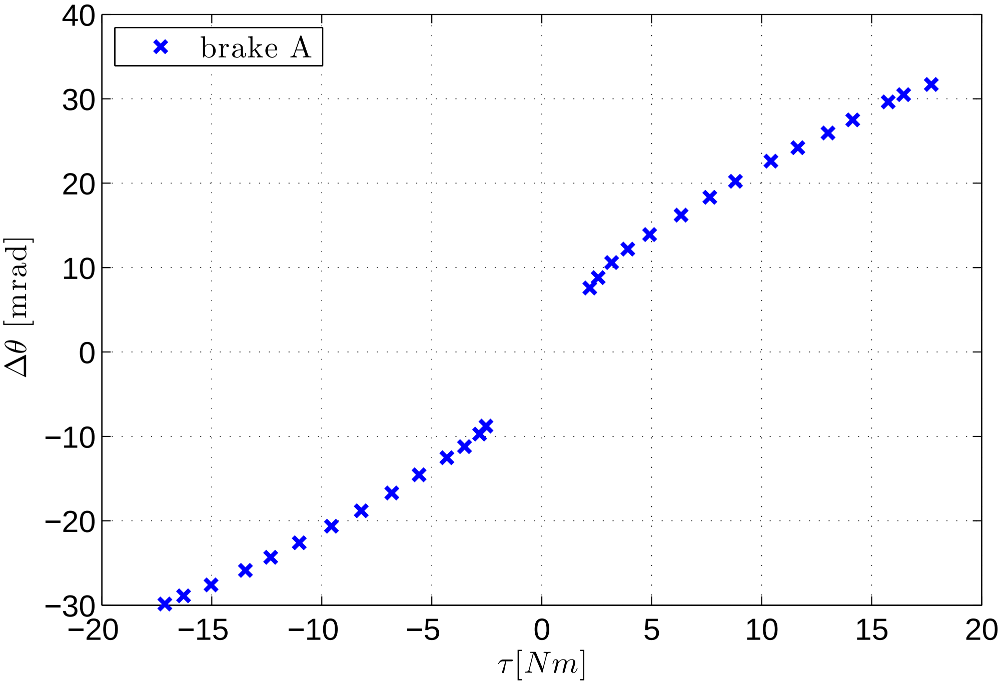

Figure 4.30: Measured joint flexibility in joint B

look-up table.

In both tested joints, this modelling is only utilizable for testing and fault detection, since each joint provides an extra position sensor on the link side of the joint, for absolute positioning. This may be different for high dynamic and high load scenarios.

Unlike the imprecise position encoding regarded earlier, flexibility, as well as friction, is not directly compensable (at least in theory), but can be taken care of in terms of controlling. The exact knowledge of the flexibility parameters then allows a sufficiently precise prediction of (elastic) material deformation for dynamic position control.

Chapter 5

Conclusion

5.1 Summary

This thesis provides an overview of the mostly used flexible robotic joint components. For the subsequent tests, the used identification setup has been presented. As one component, a magnetic rotary encoder has been tested for non-idealities. A recurring sinoid error has been found and could be compensated with a look-up table. Also, the mechanical alignment requirements, and the specified filter timing have been verified. Another non-ideality in form of a start-up initialisation error was found and attended as well. For the two joint designs, the static friction parameters have been measured for a complete parametrisation of the used static friction models. Then, these parameters were used to compensate the occurring joint friction with three different static models and one observer structure. The flexibility in the two joints was also measured and fitted in mathematical terms.

5.2 Conclusion

Analysing several parts in detail, it was clear, that most effects could be compensated, or at least be reduced with relatively small additional effort. For static non-idealities such as torque sensor shapes and the discussed rotary encoder, the ideal concept of compensation seems to be found. The shape correction improved the performance of the position encoder significantly. This method has proven itself to be ideal for such issues. Unlike that, more random non-idealities are to complex for such easy compensation methods. Static friction models as presented are not suitable yet for effective friction compensation, but with further model optimisation, it may be worth further consideration. The observer works well, but has still a higher potential, for example might a more complex structure provide significantly better results. The measurement of flexibility in robotic joints was proven to be sufficient for the given joints. For designs with such high flexibility, it is important, that the mechanical structure either provides a linear torsion behaviour, or the controlling is able to handle very complex terms to predict flexibility based vagueness, so that the effects could be considered.

5.3 Outlook

Some regarded non-idealities, such as the friction compensation still leave room for improvement. The next step here should be focussing on slow speeds. This should lead to more precise positioning and better controller performance in this case. The static friction models could be enhanced by a torque-dependent term, and/or an additional observer in the loop. Furthermore, dynamic friction models could be consulted, as they are able to model occurring elastic restoring forces. Therefore, the position precision might have to be enhanced. The main focus hereby should be lain on the critical slow-positioning area, as it is not only the most crucial, but also the most faulty part of the control. For the assembly of multiple robotic joints, the flexibility analysis becomes much more important. Because of the rising complexity, the flexibility needs to be analysed separately for multi-joint-concepts, including not only the joints itself, but the structural parts in between.

List of Abbreviations

BLDC	brushless direct current
CPU	central processing unit
DCRM	distance coded reference marks
DSP	digital signal processor
DTC	direct torque control
FOC	field oriented control
HTL	high threshold logic
IC	integrated circuit
LDR	light dependent resistor
LED	light-emitting diode
MCB	Motor Control Board
pHRI	physical human-robot interaction
QEP	quadrature encoder pulse
SNR	signal-to-noise ratio
SPI	serial peripheral interface
SSI	synchronous serial interface
SWG	strain wave gear
TTL	transistor–transistor logic
UART	Universal Asynchronous Receiver Transmitter

List of Symbols

symbol	unit	description
A, B	binary	QEP signals
X, Z	binary	QEP index signals
τ	Nm	torque
f	N	force
ϕ	°	torsion
θ	rad	position (motor position in link coordinates)
θ_d	rad	desired position
θ_m	rad	position (motor position in motor coordinates)
q	rad	position (link position in link coordinates)
$\tilde{\theta}$	rad	measured position
$\dot{\theta}$	rad/s	velocity (angular)
$\dot{\theta}_d$	rad/s	desired velocity (angular)
i_a, i_b, i_c	A	motor phase currents
i_d, i_q	A	transformed motor current (d/q-transformed)
k_m	Nm/A	motor torque constant
η	1	efficiency
ξ	rad	mechanical offset of two rotary encoders on same axis
ω	rad/s	angular velocity
μ	1	friction coefficient
ϑ	$°K$ or $°C$	temperature
f_f	N	friction force
τ_f	Nm	friction torque
f_h	N	stiction
τ_h	Nm	stiction
f_{sl}	N	limited static friction force
f_v	N	viscous friction
τ_v	Nm	viscous friction torque
f_c	N	coulomb friction
τ_c	Nm	coulomb friction

symbol	unit	description
c_v	Nm s/rad	viscous friction gradient
τ_l	Nm	load torque
f_e	N	external force
τ_s	Nm	Stribeck Effect torque
v_s	rad/s	Stribeck velocity
δ_s	1	stribeck parameter
$\sigma_.$	various	parameters for dynamic friction models
$p_.$	rad	position controlling error
β_{tr}	1	gear ratio
k	Nm/rad	stiffness
$\tilde{k}$	Nm/rad	measued stiffness
β_0	rad	directional offset in stiffness measurement
τ_g	Nm	gravitational torque
B_m	kg m^2	motor inertia

List of Figures

1.1 State of the art lightweight robots 5

2.1 Typical QEP signal with index mark at steady velocity 10
2.2 Schematic of data acquisition chain in rotary encoder application 10
2.3 Schematic of data acquisition chain in torque sensor application 11
2.4 Schematic strain gauge. The stress direction in this picture would be horizontal 12
2.5 Coulomb friction model 13
2.6 Load-dependent friction linear (a) and square (b) 14
2.7 Viscous friction model 14
2.8 Friction model with coulomb, viscous and static friction 15
2.9 Complete static friction models with stribeck effect 16

3.1 Mechanical schematic of joint structure 20
3.2 Picture of the joint identification test bench 20
3.3 Position and speed profile for testing 21
3.4 Hysteresis brake torque-speed dependency 21
3.5 Torque at variable speed with and without transmission 23
3.6 Hysteresis brake current-torque dependency 23

4.1 Picture of the rotary encoder test bench 26
4.2 Velocity dependent shift 28
4.3 Velocity dependent shifts in comparison (filtered) 28
4.4 Error shape S2 vs. S1 30
4.5 Smoothed error shape S2 vs. S1 used for compensation 30
4.6 Schematic of position error compensation: a) direct compensation; b) compensation via error 32
4.7 Schematic of position error compensation with velocity consideration . . 32
4.8 Error distribution over one revolution 33
4.9 Error distribution over one revolution with applied shape correction . . . 33
4.10 Histogram: Error distribution 34
4.11 Histogram: Error distribution over one revolution with applied shape correction 34
4.12 Speed profile used for static friction identification 35

4.13 Static friction curve of joint A 36
4.14 Static friction curve of joint B 36
4.15 Measured friction with coulomb and viscous friction modelled for joint A 37
4.16 Measured friction with coulomb and viscous friction modelled for joint B 38
4.17 Measured friction with complete static friction model for joint A 39
4.18 Measured friction with complete static friction model for joint B 39
4.19 Schematic of the implemented friction compensation structure 40
4.20 Position and speed profile for compensation evaluation 40
4.21 Reference trajectory for comparison (without any friction compensation) [joint A] 42
4.22 Ideal coulomb friction model (a); with simple avoidance of the critical discontinuation (b); and leap-less model adaptation (c) 42
4.23 Friction compensation with coulomb friction model (c) 43
4.24 Ideal friction model with coulomb and viscous friction (a) and leap-less model adaptation (b) 43
4.25 Friction compensation with coulomb-and-viscous friction model (b) . . . 44
4.26 Observer control structure 45
4.27 Friction observer schematic 45
4.28 Control error with friction observer compensation 46
4.29 Measured joint flexibility in joint A 50
4.30 Measured joint flexibility in joint B 50

List of Tables

3.1 Mechanical overview of the joint test bench 22
3.2 Mechanical overview of both identified joints 24

4.1 Comparison of both rotation encoders 26
4.2 Disparity caused by time difference 27
4.3 Disparity caused by filter runtime 29
4.4 Measured positions 31
4.5 Fitted model parameters for the coulomb and viscous friction friction models 37
4.6 Fitted model parameters for the complete static friction model 41
4.7 Overview of positioning precision with different friction compensation methods 47
4.8 Fitted stiffness parameters for joint flexibility in joint A and joint B 49

Bibliography

[1] A.W. Scheer. *Industrie 4.0*. IMC AG, 2013.

[2] A. De Santis, B. Siciliano, A. De Luca, and A. Bicchi. An atlas of physical human-robot interaction. *Mechanism and Machine Theory*, 43(3):253–270, 2007.

[3] J. Dumahel. Rethink Robotics: Finding a Market. *Stanford CasePublisher*, 2013.

[4] T. Bauernhansl, M. Hompel, and B. Vogel-Heuser. *Industrie 4.0 in Produktion, Automatisierung und Logistik: Anwendung · Technologien · Migration*. Springer Fachmedien Wiesbaden, 2014.

[5] G. Hirzinger. Mechatronics for a new robot generation. *Mechatronics, IEEE/ASME Transactions on*, 1(2):149–157, June 1996.

[6] T. Lens and O. von Stryk. Design and dynamics model of a lightweight series elastic tendon-driven robot arm. In *Robotics and Automation (ICRA), 2013 IEEE International Conference on*, pages 4512–4518, 2013.

[7] G. Hirzinger, A. Albu-Schäffer, M. Hahnle, I. Schäfer, and N. Sporer. On a new generation of torque controlled light-weight robots. In *Robotics and Automation, 2001. Proceedings 2001 ICRA. IEEE International Conference on*, volume 4, pages 3356–3363, 2001.

[8] B. Gombert, G. Hirzinger, G. Plank, and M. Schedl. Modular concepts for a new generation of light weight robots. In *Industrial Electronics, Control and Instrumentation, 1994. IECON '94., 20th International Conference on*, volume 3, pages 1507–1514, 1994.

[9] D. Grenier, L-A Dessaint, O. Akhrif, and J.-P. Louis. A Park-like transformation for the study and the control of a nonsinusoidal brushless DC motor. In *Industrial Electronics, Control, and Instrumentation, 1995., Proceedings of the 1995 IEEE IECON 21st International Conference on*, volume 2, pages 836–843 vol.2, Nov 1995.

[10] R. A. Guinee. *Electric Vehicle - Modelling and Simulations*, chapter Mathematical Modelling and Simulation of a PWM Inverter Controlled Brushless Motor Drive System from Physical Principles for Electric Vehicle Propulsion Applications. InTech, 2011.

[11] K.H. Harib, E.A. Khousa, and A. Ismail. Field Oriented Motion Control of a 3-phase Permanent Magnet Synchronous Motor. In *Electric Power and Energy Conversion Systems (EPECS), 2011 2nd International Conference on*, pages 1–7, 2011.

[12] M. Lazor and M. Stulrajter. Modified field oriented control for smooth torque operation of a bldc motor. In *ELEKTRO, 2014*, pages 180–185, May 2014.

[13] Uwe Baader. *Die direkte Selbstregelung (DSR): e. Verfahren zur hochdynamischen Regelung von Drehfeldmaschinen*. VDI-Verl., als ms. gedr. edition, 1988.

[14] Tae-Hyung Kim and M. Ehsani. Sensorless control of the BLDC motors from near-zero to high speeds. *Power Electronics, IEEE Transactions on*, 19(6):1635–1645, Nov 2004.

[15] A.H. Niasar, H. Moghbeli, and E.B. Kashani. A low-cost sensorless bldc motor drive using one-cycle current control strategy. In *Electrical Engineering (ICEE), 2014 22nd Iranian Conference on*, pages 659–664, May 2014.

[16] F. Aghili, M. Buehler, and J.M. Hollerbach. Development of a high performance direct-drive joint. In *Intelligent Robots and Systems, 2000. (IROS 2000). Proceedings. 2000 IEEE/RSJ International Conference on*, volume 3, pages 2151–2158 vol.3, 2000.

[17] A. Lauletta. The Basics of Harmonic Drive Gearing. *Gear Product News Magazine*, pages 32–36, April 2006. available online: `http://www.gearproductnews.com/issues/0406/harmonic_drive_gearing.pdf`, accessed on May 20, 2015.

[18] C.W. Kennedy and J.P. Desai. Estimation and modeling of the harmonic drive transmission in the Mitsubishi PA-10 robot arm. In *Intelligent Robots and Systems, 2003. (IROS 2003). Proceedings. 2003 IEEE/RSJ International Conference on*, volume 4, pages 3331–3336 vol.3, 2003.

[19] W. Oster, D. Pingel, and B. Sauer. *Riementriebe: Vorhaben Nr. 68 dynamisches Verhalten von Riementrieben ; Abschlußbericht*. Forschungshefte // Forschungskuratorium Maschinenbau. FKM, 1983.

[20] Chunsheng Yang. Design optimization of belt transmission by intelligent algorithm. In *Computational Intelligence and Software Engineering, 2009. CiSE 2009. International Conference on*, pages 1–4, Dec 2009.

[21] H.M. Hiersig. *Lexikon Maschinenbau*. VDI-Buch. Springer Berlin Heidelberg, 1995.

[22] R. Skutsch. *Zwei Vorträge über die Mechanik der Riementriebe*. Steffen, 1986.

[23] H. Walcher. *Winkel- und Wegmessung im Maschinenbau*. VDI-Verlag, 1985.

[24] E. Ramsden. *Hall-Effect Sensors: Theory and Application*. Elsevier Science, 2011.

[25] Seung-Ho Jeong, Se-Hyun Rhyu, Byung-Il Kwon, and Byung taek Kim. Design of the rotary magnetic position sensor with the sinusoidally magnetized permanent magnet. *Magnetics, IEEE Transactions on*, 43(4):1837–1840, April 2007.

[26] S. Ekelof. The genesis of the wheatstone bridge. *Engineering Science and Education Journal*, 10(1):37–40, Feb 2001.

[27] H.B. Wang and Z.H. Feng. A highly sensitive magnetometer based on the villari effect. *Magnetics, IEEE Transactions on*, 49(4):1327–1333, April 2013.

[28] LeTien L. Decoupling control and friction compensation for robot with elastic coupled joints. *at - Automatisierungstechnik*, 2010.

[29] LeTien L. *Ansätze zur entkoppelten Regelung von mechanisch gekoppelten Doppelgelenken eines DLR-Medizinroboters*. Dissertation, Technische Universität Dresden, 2010.

[30] H. Olsson, K. J. Åström, M. Gäfvert, C. Canudas De Wit, and P. Lischinsky. Friction models and friction compensation. *Eur. J. Control*, 1998.

[31] B. Bona and M. Indri. Friction compensation in robotics: an overview. In *Decision and Control, 2005 and 2005 European Control Conference. CDC-ECC '05. 44th IEEE Conference on*, pages 4360–4367, Dec 2005.

[32] L.X. Anh. *Dynamics of Mechanical Systems with Coulomb Friction*. Computational fluid and solid mechanics. Springer, 2003.

[33] Stribeck R. *Die wesentlichen Eigenschaften der Gleit- und Rollenlager*. Mitteilungen über Forschungsarbeiten auf dem Gebiete des Ingenieurwesens, insbesondere aus den Laboratorien der technischen Hochschulen. Julius Springer, 1903.

[34] P.S. Gandhi, F.H. Ghorbel, and J. Dabney. Modeling, identification, and compensation of friction in harmonic drives. In *Decision and Control, 2002, Proceedings of the 41st IEEE Conference on*, volume 1, pages 160–166 vol.1, Dec 2002.

[35] M. Oueslati, R. Bearee, O. Gibaru, and G. Moraru. Improving the dynamic accuracy of elastic industrial robot joint by algebraic identification approach. In *Systems and Computer Science (ICSCS), 2012 1st International Conference on*, pages 1–6, Aug 2012.

[36] Harnoy A. and Friedland B. Dynamic friction model of lubricated surfaces for precise motion control. In *Society of Tribologists and Lubrication Engineers*, 1993.

[37] D. Chou. *Dahl Friction Modeling*. Massachusetts Institute of Technology, Department of Mechanical Engineering, 2004.

[38] C.C. De Wit, H. Olsson, K.J. Astrom, and P. Lischinsky. A new model for control of systems with friction. *Automatic Control, IEEE Transactions on*, 40(3):419–425, Mar 1995.

[39] G. Ferretti, G.A. Magnani, and P. Rocco. Single and multistate integral friction models. *Automatic Control, IEEE Transactions on*, 49(12):2292–2297, Dec 2004.

[40] Sebastian Dendorfer. *Ein modularer Prüfstand für Antriebseinheiten*. Semesterarbeit, Technische Universität München, 2013.

[41] D. Schröder. *Intelligent Observer and Control Design for Nonlinear Systems*. Springer, 2000.

[42] G. Ellis. *Observers in Control Systems: A Practical Guide*. Elsevier Science, 2002.

[43] A. Albu-Schäffer. *Regelung von Robotern mit elastischen Gelenken am Beispiel der DLR-Leichtbauarme*. PhD thesis, Technischen Universität München, 2002. (German).

[44] Walther S. *Modeling, Identification, and Control of a Mechanically Coupled 2-DoF Torque Controlled Lightweight Joint*. Diplomarbeit, Technische Universität München, 2012.